MATERIALS CHEMISTRY FRONTIERS

RESEARCH ARTICLE

View Article Online
View Journal | View Issue

Cite this: *Mater. Chem. Front.*, 2025, **9**, 3425

Humidity-tolerant selective sensing of hydrogen and *n*-butanol using ZIF-8 coated CuO:Al film

Rajat Nagpal,[ab] Masaya Sugihara,[c] Nicolae Magariu,[b] Tim Tjardts,[d] Nahomy Meling-Lizarde,[d] Thomas Strunskus,[de] Tayebeh Ameri,*[de] Rob Ameloot,[c] Rainer Adelung[ae] and Oleg Lupan*[b]

Hydrogen and *n*-butanol are emerging as clean energy carriers, necessitating reliable sensors for their low concentration detection. This study investigates an aluminium-doped CuO (CuO:Al) sensor coated with a zeolitic imidazolate framework-8 (ZIF-8) layer for hydrogen and *n*-butanol detection. Comprehensive characterization was performed using X-ray diffraction (XRD), X-ray photoelectron spectroscopy (XPS), scanning electron microscopy (SEM), energy-dispersive X-ray spectroscopy (EDX), thermogravimetric analysis (TGA), N_2-adsorption isotherms, and Raman spectroscopy, collectively confirming a crystalline structure, intact chemical composition, beneficial surface morphology, uniform metal–organic framework (MOF) particle distribution, hierarchical porosity, and a high thermal stability of the synthesized materials. CuO promotes interaction with hydrogen and *n*-butanol, while the ZIF-8 coating enhances selectivity by mitigating the sensitivity to other gases and confers high immunity to elevated relative humidity (RH 81%) for hydrogen gas sensing. The hybrid MOF-ZIF-8/CuO:Al (ZIF-8 coated CuO:Al) sensor demonstrates remarkable thermal and temporal stability and maintains consistent performance even in humid conditions. Electrical activation energy (~0.2 eV), corresponding to hole trap state (V_{Cu}), was calculated, confirming the p-type conduction mechanism. A gas sensing response of 400% was observed for 1000 ppm hydrogen gas under low relative humidity (RH 11%), remaining stable over four weeks. The gas sensing response remained at 300% even at a higher relative humidity (RH 50%) and sustained a response of 200% even after four weeks under the same RH. This shows its potential for hydrogen detection in industrial safety, environment monitoring, clinical medical diagnosis, and its reliable deployment in hydrogen generated energy applications.

Received 30th July 2025,
Accepted 6th October 2025

DOI: 10.1039/d5qm00565e

rsc.li/frontiers-materials

Introduction

As the world population has increased dramatically in last few centuries, it is expected to add two billion more in current population (~8 billion) in next three decades.[1] Thus, it is required to increase the global energy production and its efficiency to meet the upcoming energy requirements. The data shows global energy demand may increase from 671.5 quadrillion Btu (British thermal unit) to 769.8 quadrillion Btu in the next decade.[2] The utilization of clean energy sources such as Bio-butanol and hydrogen can become key contributors to meet the global energy requirements and maintaining climate neutrality in upcoming decades.[3] Bio-butanol demonstrates high fuel standards like high hydrogen-to-carbon ratio, presence of high oxygen content,[4] which are compatible with internal combustion engines.[5] The use of a highly fuel-efficient modern diesel engine (operated by compression ignition) as compared to a gasoline engine (operated by spark ignition) is a way towards energy saving. The high environmental pollution caused by diesel engines is a major obstacle to their widespread use in diverse applications. However, the facile method of butanol blending with diesel lowers the particulate matter and NO_x emission mani-folds.[6] Butanol is highly volatile, which can be harmful to the environment as well as to human health.[7] Thus, efficient sensors are essential for the real-time monitoring of vaporized *n*-butanol in industries and laboratories.[8]

Hydrogen is rapidly emerging as a cornerstone of the clean energy transition due to its zero carbon emissions and high

[a] *Functional Nanomaterials, Department of Materials Science, Faculty of Engineering, Kiel University, Kaiserstr. 2, D-24143, Kiel, Germany*
[b] *Department of Microelectronics and Biomedical Engineering, Center Nanotechnology and Nanosensors, Technical University of Moldova, 168 Stefan cel Mare Av., MD-2004 Chisinau, Republic of Moldova. E-mail: ollu@tf.uni-kiel.de, oleg.lupan@mib.utm.md*
[c] *Center for Membrane Separations, Adsorption, Catalysis, and Spectroscopy, KU Leuven, 3001 Leuven, Belgium*
[d] *Chair for Composite Materials, Department of Materials Science, Faculty of Engineering, Kiel University, Kaiserstr. 2, D-24143, Kiel, Germany. E-mail: tam@tf.uni-kiel.de*
[e] *Kiel Nano, Surface and Interface Science KiNSIS, Kiel University, Christian Albrechts-Platz 4, 24118, Kiel, Germany*

gravimetric energy density, offering a sustainable and environmentally friendly alternative to fossil fuels.[9] It holds immense promise to decarbonize various systems, such as fuel cells,[10] industrial processes,[11] and energy storage systems.[12] However, hydrogen has safety risks in its production and transportation due to its explosive, flammable nature, as well as the difficulty in detecting leaks with natural human senses alone.[9] Thus, it is critical to develop effective sensing technology to ensure its safe handling to use it as versatile source of energy. Currently, a lot of hydrogen sensing technologies are being applied to enhance the sensitivity and selectivity[13–15] of hydrogen in diverse environments containing volatile organic compounds (VOCs),[16] ammonia,[17] and moisture.[18]

Chemoresistive gas sensors are crucial for low-cost and high response solid-state gas sensors. Around 20% of the used materials are based on metal-oxides which operate in the presence of oxygen.[19] One promising candidate as sensing material is CuO, which is widely used to detect VOCs,[20,21] and a lot of other reducing analytes[22] due to its p-type semiconducting property,[23] narrow band gap,[24] large surface area,[25] cost-effectiveness,[26] and abundance.[27] Furthermore, CuO as a p-type metal oxide semiconductor, forms an insulating core and a hole accumulation layer upon adsorption of anionic species.[28] After exposure of reducing gas on its surface, the interaction of reducing gases with adsorbed oxygen anions lead to the recombination of holes and electrons, which reduces the hole concentration, and increases the resistance of CuO.[29]

Various studies have explored CuO-based gas sensors due to their promising sensing properties. For example, Zhou *et al.*[30] reported a highly sensitive porous gas sensor based on CuO/Cu_2O mixed phases for the detection of acetone. However, reports on hydrogen detection using bare CuO remain scarce. Hoa *et al.*[31] addressed this gap by synthesizing CuO nanowires on porous single-walled carbon nanotubes, achieving hydrogen sensing response ($\sim$400%) at 250 °C for 6% hydrogen following high-temperature oxidation treatment. Numerous studies have investigated VOCs and hydrogen sensing using mixed metal oxide systems. Lupan *et al.* demonstrated the selective detection of hydrogen and *n*-butanol through surface functionalization of TiO_2/CuO/Cu_2O structures with noble metals.[32,33] Their work showed that Pd functionalization of TiO_2/CuO/Cu_2O structures could detect hydrogen concentrations as low as 5 ppm, while Ag and AgPt functionalization enabled selective sensing of *n*-butanol molecules.[33] Without surface functionalization, TiO_2/CuO/Cu_2O structures showed ethanol selectivity.[32] One of the latest published works based on nano-patterned CuO nanowire-based hydrogen sensors have demonstrated a sensing response of $\sim$200% at 300 °C for a concentration of 5000 ppm.[34] The doping effect in metal oxide semiconductors plays a crucial role in modulating gas sensing performance. In CuO, donor doping reduces the hole concentration, resulting in an increased electrical resistance.

Metal doping significantly influences the surface properties. For instance, the lattice mismatch between Al^{3+} (0.53 Å) and the lattice cation Cu^{2+} (0.73 Å) induces changes in morphology and surface area, likely due to the formation of defect states within the lattice.[35] A study by Yoo *et al.* reported the effect of Al doping on the gas sensing performance of ZnO/CuO.[36] It demonstrated that the response towards ammonia increases drastically by increasing the local concentration of ammonia for the Al-doped ZnO/CuO heterojunction compared to the undoped ZnO/CuO heterojunction.

Hydrogen detection under high-humidity conditions is critical for energy-related applications,[18] especially in environments where humidity exceeds 50% RH, such as urban areas in the United States[37] and polar regions of Europe and the North Atlantic coastal region.[38] This requirement extends to electronics manufacturing facilities, where humidity typically ranges from 30% to 70% depending on process specifications.[39] Given hydrogen's extensive use in semiconductor processing,[39] reliable leak detection in these settings is essential for operational safety and process integrity.[40]

For instance, Lupan *et al.* conducted a study on Al_2O_3 coated CuO film for hydrogen detection at high RH.[41] In this study, a sensor was fabricated by depositing CuO using sample synthesis from chemical solutions (SCS), followed by a deposition of a 6 nm thick Al_2O_3 layer using atomic layer deposition (ALD). This approach enabled detection of hydrogen concentrations as low as 5 ppm, even at high RH of 84%.[41] While noble metal doping (*e.g.*, Pt, Pd, or Rh) typically enhances metal oxide selectivity through catalytic action, studies indicate compromised selectivity in SnO_2-based sensors under high humidity.[42] This limitation arises from competitive interactions between hydrogen and water molecules at surface reaction sites.

Selectivity is also a crucial parameter in gas sensing. Bare metal oxides generally face challenges with selectivity.[19] However, coating metal oxides with MOFs can mitigate this issue. MOFs are highly flexible framework structures due to their tunable pore sizes which lead to a molecular sieving effect.[43] Numerous studies have reported on MOFs and MOF-derived metal oxides for sensing and related applications.[44,45] For instance, ZIF-8 is a class of MOFs porous materials consisting of Zn ions as metal nodes and 2-methylimadazolate as an organic linker. Its three-dimensional framework, composed of organic linkers and inorganic metal nodes, exhibits a sodalite topology and features a nominal aperture size of 3.4 Å and a pore diameter of 11.6 Å.[46] The molecular sieving effect of ZIF-8 allows gas molecules with smaller kinetic diameters, such as hydrogen (2.89 Å),[47] to pass through it and makes it difficult for larger molecules, such as acetone (4.6 Å)[47] and ethanol (4.53 Å)[47] to pass through, resulting in highly selective hydrogen detection.[48]

Organic MOFs can be deposited onto inorganic metal oxide–semiconductor based interdigitated electrode (IDE) devices using a variety of methods, including controlled deposition techniques (such as Langmuir–Blodgett) and manual techniques (such as spin-coating, dip-coating, or drop-casting).[49] Although *in situ* growth can be advantageous in terms of direct integration, it often requires sophisticated synthesis setups. Alternatively, MOF-layer transfer techniques, including Langmuir–Blodgett deposition, may introduce structural defects or poor adhesion to the substrate during the transfer process.[50]

On the contrary, drop-casting offers a simple, cost-effective, and accessible approach for depositing MOF particles between the IDE fingers.[51] However, this method may lead to non-uniform coverage and limited spatial control over a distribution of MOF particles. While repeated iteration on a target region can improve coverage uniformity, it may simultaneously preserve the sensor's overall good conductivity.[52]

In this research, we present an Al-doped CuO gas sensor functionalized with MOFs ZIF-8 for highly selective hydrogen sensing under various environmental conditions, as well as for the selective detection of *n*-butanol among a set of gases commonly referred to as ABE (acetone, *n*-butanol, and ethanol). The proposed sensor fabrication process involves the formation of the CuO:Al grains followed by drop-casting a dispersion of ZIF-8 nanoparticles onto the surface. The fabricated hybrid sensor shows thermal and temporal stability even in the presence of 50% humidity. When compared with existing literature, this work is novel in terms of ZIF-8/CuO:Al based structure for hydrogen detection with unprecedented selectivity (>4 times), long-term stability of about four weeks, and quick response/recovery times in the presence of humidity.

Experimental

CuO:Al films were synthesized on the glass substrates (12 mm × 14 mm × 1 mm).[53,54] The glass substrates were pre-cleaned using HNO_3 (30%) followed by rinsing in deionized (DI) water. The purpose of cleaning with HNO_3 is to remove organic contaminants. Afterwards, the glass substrates were cleaned with ethanol and acetone to remove hydrophilic acid residues left after the first step of cleaning. A solution of a copper thiosulfate complex was used as a cationic precursor, consist of 1 mol L^{-1} of copper sulphate pentahydrate (>99%, Ecochimie SRL) and 1 mol L^{-1} of sodium thiosulfate pentahydrate (>98.5%, Ecochimie SRL). Under continuous stirring at room temperature, the solution was diluted with DI water to 0.1 mol L^{-1}. Al doping was carried out by adding 10 mg of aluminium nitrate hexahydrate ($Al(NO_3)_3 \cdot 9H_2O$, Alfa Aesar) dissolved in 100 ml of DI water to the diluted solution.[55] Similarly, under continuous stirring at 80 °C, an anionic precursor was prepared using 2 mol L^{-1} of sodium hydroxide (>99%, Ecochimie SRL) in DI water.

The pre-cleaned sample was immersed in the prepared precursor solutions using an articulated robot, which has been programmed to immerse the sample for 3 seconds (s) and 6 s in the cationic precursor and the anionic precursor solution, respectively. The above process is repeated for 75 number of cycles using an articulated robot to avoid human errors in dipping time and repetability.[53] The sample was dried under a dry air flux after successful deposition of the CuO:Al film. Afterwards rapid thermal annealing (RTA) was performed at 600 °C for 60 s to enhance the crystallinity of the thin film, as previously reported.[54]

ZIF-8 dispersion was prepared as follows. 297.49 mg (1 mmol) of zinc nitrate hexahydrate (99%, Fisher Chemical) and 328.40 mg (4 mmol) of 2-methylimidazole (99%, Sigma-Aldrich) were dissolved separately in 20 mL of methanol (≥99%, Fisher Chemical) each. The latter solution was rapidly added to the former solution under stirring for 1 minute. After 24 hours, white solids were separated from the dispersion by centrifugation, followed by washing two times with methanol and one time with 2-propanol (≥99.5%, Sigma-Aldrich). The resultant powder was kept in 2-propanol to prevent aggregation.

Following established protocols,[56] Au electrodes with a 1 mm gap were fabricated on the CuO:Al film to serve as electrical contacts before the deposition of ZIF-8 nanoparticles. The prepared dispersion (3000 μl) containing ZIF-8 at a concentration of 0.75 mg mL^{-1} was ultrasonicated for 15 minutes, followed by drop-casting approximately 100 μl on the CuO:Al film using micropipette. The schematic for illustrating the fabrication process of ZIF-8/CuO:Al film on the glass substrate is shown in Fig. 1.

XRD measurements were performed using a Rigaku diffractometer equipped with a high-flux X-ray source (9 kW) and Cu-Kα1 radiation (1.54 Å) in parallel beam (PB) configuration within a 2θ range of 5–100° with a step size of 0.05°. The thin-film XRD unit operated at 45 kV and 200 mA to capture the diffraction pattern. HyPix-3000 high photon counting (HPC) 1D detector (line mode) was used to acquire high resolution diffraction data, for capturing a highly sensitive signal with low noise performance. The morphological studies of the ZIF-8/CuO:Al samples were done using SEM using a Zeiss system at 7 kV and 10 μA, equipped with an EDX detector used for elemental mapping and compositional analysis. Raman spectra of the samples were acquired using an alpha300 RA micro-Raman spectrometer (WITec GmbH, Ulm, Germany) equipped with a triple grating system, a charge coupled device (CCD) detector with grating parameters set at 600 grooves mm^{-1} with a blaze wavelength of 500 nm. A green Nd:YAG laser with a wavelength of 532 nm was used as the source with an optical power of 8 mW.[41,57] Calibration of the spectrometer was done using a silicon standard with a known peak at around 521 cm^{-1}. Nitrogen physisorption on bulk ZIF-8 powder was performed at 77 K using a Micromeritics 3Flex 3500 instrument. Prior to the physisorption measurement, the sample was degassed at 140 °C under vacuum for 12 hours. Thermogravimetric analysis (TGA) was performed using a STA 449 F3 Jupiter instrument (Netzsch, Germany) under a flow of synthetic air at a flow rate of 50 mL min^{-1}. The measurement was carried out over a temperature range of 25 °C to 800 °C with a constant heating rate of 5 °C min^{-1}. Elemental surface analysis of the ZIF-8/CuO:Al and CuO:Al films was performed using an XPS ultra-high vacuum (UHV) system (PREVAC sp. z o. o.) equipped with a non-monochromatic Al Kα excitation X-ray source (1486.6 eV) operated at 300 W (15 kV, 20 mA). The base pressure inside the XPS analysis chamber was maintained in the 1×10^{-8} to 1×10^{-9} mbar range, which was provided by a turbomolecular pump and a scroll backing pump. Survey spectra were measured over a binding energy range from 0 to 1300 eV for three samples the CuO:Al (reference sample), the ZIF-8/CuO:Al (partially covered with ZIF-8 coating at a low concentration of ~50 μl and almost completely covered with ZIF-8 coating at a concentration of ~100 μl) with three iterations and a pass energy of 200 eV.

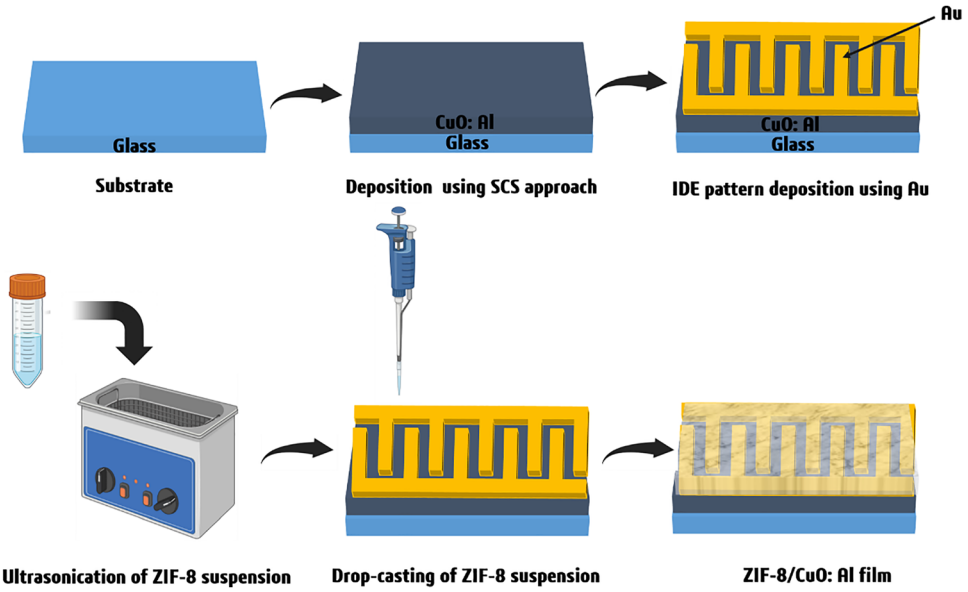

Fig. 1 Schematic illustration of the stepwise fabrication process for the organic–inorganic metal–organic frameworks ZIF-8/CuO:Al film-based hybrid sensor.

High-resolution spectra were acquired in the relevant binding energy regions using twenty iterations and a pass energy of 50 eV. XPS spectra were analyzed using Casa XPS version 2.3.23. A Gaussian–Lorentzian line shape (1 : 1) was used as the fitting function for peak analysis and the background was corrected using the Shirley algorithm. Due to differential surface charging in the ZIF-8 layers, the binding energies were calibrated against the Zn $2p_{3/2}$ line of ZIF-8 at 1021.7 eV, as reported in the literature.[58] For calculating the chemical surface composition, numerical integration of the spectra with the Shirley background subtraction and application of the corresponding relative sensitivity factors were utilized.

The prepared samples were exposed to a range of test gases and VOCs (hydrogen, *n*-butanol, 2-propanol, ethanol, acetone, and ammonia) with a concentration of 100 ppm in air at different operating temperatures (OPTs) in a range from 150 °C to 350 °C at an interval of 50 °C. The sensing setup consisted of a gas flow system (carrier gas, bubbler, target analyte, and mass flow controllers (MFCs)), a closed chamber (sample platform, electrodes, gas inlet and outlet ports, and temperature control), and a Keithley source meter 2400, controlled *via* LabView interface.

The test gas was diluted to 100 ppm by mixing air using MFCs.[55] The concentration (C') can be calculated using the formula:

$$C' = \frac{C'' \times F_a}{F_t} \quad (1)$$

where C'' is the concentration of the test gas in the bottle, F_a is the flow rate of analyte, and F_t is the flow rate of the mixture of test gas and air.

The gas flow rates of both gases (F_a and F_t) in the closed chamber were kept at 200 standard cubic centimetres per minute (sccm) using MFCs.

A heater was placed below the sample in which the temperature was controlled using a microcontroller. Samples were tested in the presence of test gases at RH 11% and RH 50%, measured using a hygrometer, as previously reported.[54] Using a bubbling system, by passing a carrier air through water at room temperature, higher RH was generated and injected into a closed chamber. To investigate the electrical properties of tested sample, a two-point probe was used.

The gas sensing response (S) was determined using the following relation:[32,59]

$$S\ (\%) = \frac{R_{gas} - R_{air}}{R_{air}} \times 100\% \quad (2)$$

where R_{air} is the resistance of the sample in air and R_{gas} is the resistance of the sample during gas exposure. The error bar represents 10% of the gas response value.

The response time is defined as the time required for the sensor to reach 90% of the total change in resistance upon exposure to the target gas. Conversely, the recovery time is the time required for the sensor to return to 10% of the total resistance change after the gas is removed, as it approached its baseline resistance.

Results and discussion

Structural properties

Fig. 2 shows an indexed XRD pattern of the ZIF-8/CuO:Al film-based heterostructure. The primary peaks of the pattern are at 2θ angles of 38.81° and 35.56°. They strongly suggest that the ZIF-8/CuO:Al film is composed of a CuO phase as they respectively match with the (1 1 1) and (1 1 $\bar{1}$) lattice planes of the monoclinic CuO pdf map 1526990 reference. Furthermore, several peaks at higher 2θ angles match with this reference as well which clearly indicates monoclinic CuO to be present in the ZIF-8/CuO:Al film-based hybrid structure. Additionally, the diffractogram in Fig. 2 displays six peaks corresponding to Au used as top-electrode. This was confirmed by the pdf map no.

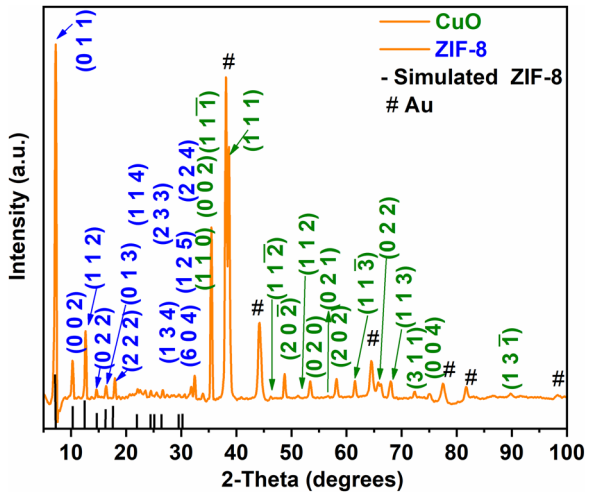

Fig. 2 XRD pattern of the ZIF-8/CuO:Al film-based structure with Au contacts. The diffraction peaks are indexed to CuO (green), ZIF-8 (blue), and Au used for electrical contacts (indicated by the symbol "#"). The black bars represent the simulated reference pattern corresponding to the ZIF-8 phase.

1100138. The Au peaks present in the diffraction pattern are due to the Au electrical connections for the measurements. Multiple ZIF-8 peaks were observed in the 2θ range from 7° to 32°. The positions of all MOF ZIF-8 peaks were confirmed using a simulated reference pattern obtained from a crystallographic information file (CIF).[60] The highest intensity reflection was observed at 2θ = 7.20°, corresponding to (0 1 1) planes. The crystallite dimensions of ZIF-8 nanoparticles were quantitatively analysed through XRD line profile analysis using Scherrer equation.[61]

$$d = \frac{K \times \lambda}{\beta \times \cos\theta} \quad (3)$$

where d represents the crystallite size (coherent diffraction domain), K is the dimensionless shape factor (0.940 nm for cubic systems), λ denotes the Cu-Kα radiation wavelength (0.15406 nm), β corresponds to the full width at half maximum (FWHM) in radians, and θ is the Bragg angle.

The Voigt profile was chosen because it provides a best fit among the three profile functions: Gaussian, Lorentzian, and Voigt. This conclusion was reached by comparing the coefficient of determination (R^2) values, where R is the correlation coefficient for all three regression functions. The highest R^2 value, indicating the best fit, was 0.98150 for the Voigt regression function. Peak deconvolution was performed using the Voigt profile *via* orthogonal distance regression optimization, which simultaneously accounts for Lorentzian broadening (w_L) and Gaussian broadening (w_G).

The FWHM (β) of the XRD peak corresponding to the plane (0 1 1) was derived using the empirical approximation:[62]

$$\beta \approx 0.5346 \times w_L + \sqrt{0.2166 \times w_L^2 + w_G^2} \quad (4)$$

yielding $\beta = 0.0049 \pm 0.02\%$ radians. Application of the Scherrer Equation yielded an estimated crystallite size of $d \approx 30$ nm, representing the coherently diffracting domains.[63] This contrasts sharply with SEM data showing particle size ≈ 70 nm. The disparity in crystallite size calculated from the Scherrer equation and particle size estimation from SEM indicates on the polycrystalline architecture of ZIF-8 nanoparticles,[63] where macroscopic particles comprise few smaller crystallites. This structural hierarchy introduce extensive grain boundary interfaces and implies increase in defect density and active sites, which can enhance optimization pathways for sensing applications.

No Al-related phases were detected in the diffraction pattern due to low concentration of Al in films. The sharp peaks indicate the high crystallinity of the ZIF-8/CuO:Al film-based structure.

Morphological and micro-Raman properties

Fig. 3(a) shows an SEM image of the CuO:Al film with intergranular structures without ZIF-8 coating on top. It reveals highly dense triangular shaped CuO:Al grains distributed randomly without any preferential orientation. Moreover, the SEM images of the CuO:Al film at different magnifications are shown in Fig. S1. The grain distribution of the CuO:Al film can be observed using SEM, as shown in Fig. S2(a), which was used for grain size estimation. The CuO:Al grains appear to be homogeneously interconnected after thermal treatment at 600 °C for 60 s. ZIF-8 nanoparticles are uniformly distributed on the CuO:Al film. The corresponding SEM images of the ZIF-8/CuO:Al film-based structure at several magnifications are shown in Fig. 3(b)–(d), which reveal the surface morphologies of the thermally grown CuO:Al intergranular structures. The dispersion contains rhombic dodecahedral nanoparticles of MOF ZIF-8, which after drop-casting onto a Si substrate, exhibit a particle size of approximately 70 nm (Fig. S2(b)). Elemental mapping and compositional analysis of the CuO:Al film was conducted using EDX characterization, as shown in Fig. S3. SEM image from Fig. S3(a) shows the analyzed region of approximately 11.3 μm × 8.5 μm size. The results confirm the presence of Cu, O, and Al, as expected. Although the presence of Al is not confirmed by XRD due to its low doping concentration, presence

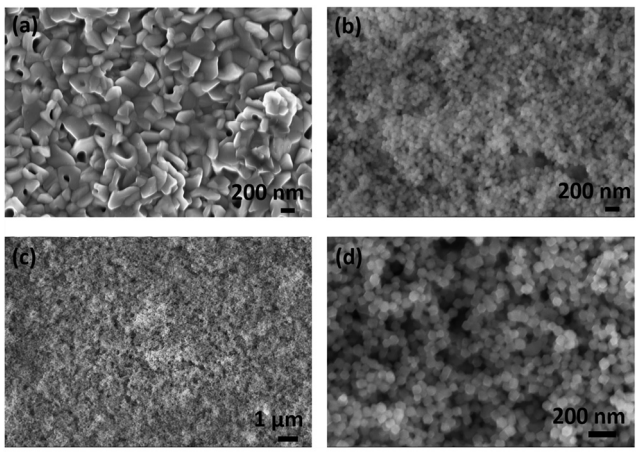

Fig. 3 (a) SEM image of the CuO:Al film. (b), (c), and (d) Low magnification and high magnification SEM images of the ZIF-8/CuO:Al films-based structure.

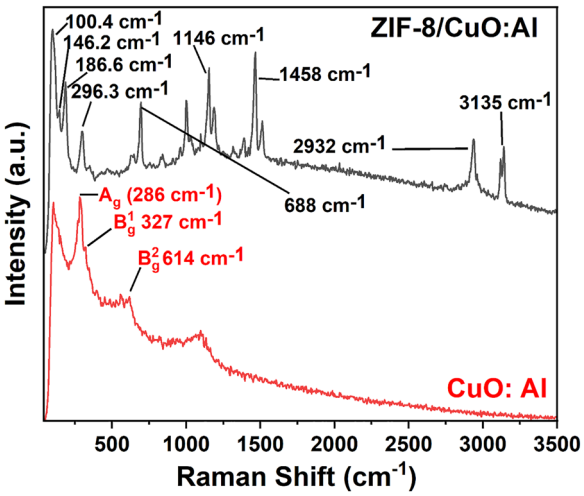

Fig. 4 Raman spectra of the ZIF-8/CuO:Al and CuO:Al films.

of Al is confirmed by the EDX measurement. EDX analysis revealed a composition of 45.5 at% Cu, 54.3 at% O, and 0.2 at% Al.

Fig. 4 shows the Raman spectrum of the ZIF-8/CuO:Al and CuO:Al films. The spectrum of monoclinic CuO displays three Raman-active modes A_g (286 cm^{-1}), B_g^1 (327 cm^{-1}), and B_g^2 (614 cm^{-1}), which matches well with the reported literature.[64] The Raman spectrum of the ZIF-8/CuO:Al film exhibits characteristic peaks in the range of 100–3500 cm^{-1}, which are not observed in the CuO:Al film. Specifically, peaks at 100.4 cm^{-1}, 146.2 cm^{-1}, and 186.6 cm^{-1} were observed, which correspond to the lattice framework of ZIF-8. Peaks at 296.3 cm^{-1}, 688 cm^{-1}, 1146 cm^{-1}, and 1458 cm^{-1} were also identified, representing strong vibrational modes. These modes are attributed to the stretching (ν) of bonds between the metal ligand and imidazole ring (Zn–N), the out-of-plane bending vibration of imidazolate ring, the C_5–N stretching vibration (ν), and the methyl bending vibration, respectively. These observed bands are consistent with the previously reported values for these vibrations, specifically 278 cm^{-1}, 686 cm^{-1}, 1146 cm^{-1}, and 1458 cm^{-1}, respectively.[65,66] A notable blue shift in the Zn–N stretching mode may be attributed to localized defects, such as missing linker or uncoordinated metal sites.[67] Additionally, two bands were observed at the higher end of the measured range, at 2932 and 3135 cm^{-1}, which correspond to the antisymmetric C–H stretching vibrations in the methyl group and the imidazole ring, respectively.[68,69] In addition to the indications given by XRD and SEM, these findings confirm that ZIF-8 retains its structure after being deposited on the CuO:Al film.

Thermal, chemical, and adsorption properties

The thermal stability of ZIF-8 powder was investigated under a synthetic air atmosphere using TGA. As shown in Fig. S4, the material exhibits negligible weight loss up to ~380 °C, indicating the absence of physisorbed solvents or ambient moisture and confirming the structural integrity of the framework within this temperature range. A pronounced mass loss was observed beyond this temperature, which is attributed to the thermal decomposition of the organic 2-methyimidazolate linkers and the subsequent collapse of the framework.[70] The decomposition process resulted in a stable residual mass of ~34.9 wt% reached at around 640 °C. This relatively stable plateau can be observed up to 800 °C, indicating the formation of thermally stable ZnO, consistent with previous studies.[71,72]

We analyzed the surface chemistry of two ZIF-8/CuO:Al films-based structures with varying ZIF-8 coverages as well as an uncoated CuO:Al reference sample *via* XPS. Here, as the two ZIF-8/CuO:Al films-based structures, a completely ZIF-8 covered CuO:Al film and a partially covered film were selected according to the details given in the experimental section. For simplicity in naming, the completely ZIF-8 covered CuO:Al film is referred to as ZIF-8/CuO:Al (high coverage) and the partially ZIF-8 covered CuO:Al film as ZIF-8/CuO:Al (low coverage). Fig. 5(a) shows the respective XPS survey spectra of all three samples with the main photoemission lines labelled accordingly. For the ZIF-8/CuO:Al (high coverage) sample, all characteristic photoelectron lines of ZIF-8-namely Zn 2p, N 1s, and C 1s were observed, and no Cu lines were visible, indicating essentially complete coverage of the CuO:Al film (Fig. 5(a)-(i)). In contrast, the ZIF-8/CuO:Al (low coverage) sample exhibited additional Cu related photoelectron features corresponding to the CuO:Al film (Fig. 5(a)-(ii)). The XPS survey spectrum of the CuO:Al reference sample only shows the expected signals from Cu, O, and C (Fig. 5(a)-(iii)). Additionally, the XPS survey scan of the CuO:Al reference and the ZIF-8/CuO:Al (low coverage) sample exhibit a small Na 1s peak which indicates residual Na from the sodium thiosulfate pentahydrate used in the CuO:Al thin film synthesis.

High resolution spectra of the ZIF-8/CuO:Al (high coverage) sample are shown in Fig. 5(b)–(e). The C 1s spectrum can be deconvoluted into two components at the respective binding energies of 287.0 eV (C 1) and 286.1 eV (C 2) (Fig. 5(b)). In the literature, C 1s spectra associated with ZIF-8 were reported with varying number of components and line positions. For instance, Liu *et al.* reported one line at 284. 8 eV,[73] while Awadalla *et al.* reported a C 1s line at 285.1 eV, if referenced to a Zn $2p_{3/2}$ line positioned at 1021.7 eV.[74] Moreover, Soliman *et al.* reported three C 1s components at 284.5 eV, 286.2 eV, and 288.8 eV.[58] Therefore, the fitting of the C 1s line and the assignments appear to be somewhat ambiguous. We assign the C 1 component at 287.0 eV to the one carbon atom bonded to two nitrogen atoms in ZIF-8 as well as carbon bonded to oxygen *via* oxidation, because we also observe a small O 1s line in the ZIF-8/CuO:Al (high coverage) sample in Fig. 5(c). Furthermore, we suggest that the C 2 component at 286.1 eV associates with the two carbons in the ZIF-8 specific imidazole ring bonded to just one nitrogen neighbour.

Fig. 5(d) shows the corresponding N 1s spectrum in which two components can be observed. We assign the more intense peak at 400.1 eV (N 1) to nitrogen in the imidazole ligand coordinated to Zn^{2+} within the ZIF-8 framework. Additionally, we allocate the lower-intensity component at 398.2 eV (N 2) to the uncoordinated 2-methylimidazole linker. Both, the N 1 and N 2 component assignment correspond to the ZIF-8 characterization study from Tian *et al.*[75] Fig. 5(e) displays the Zn 2p

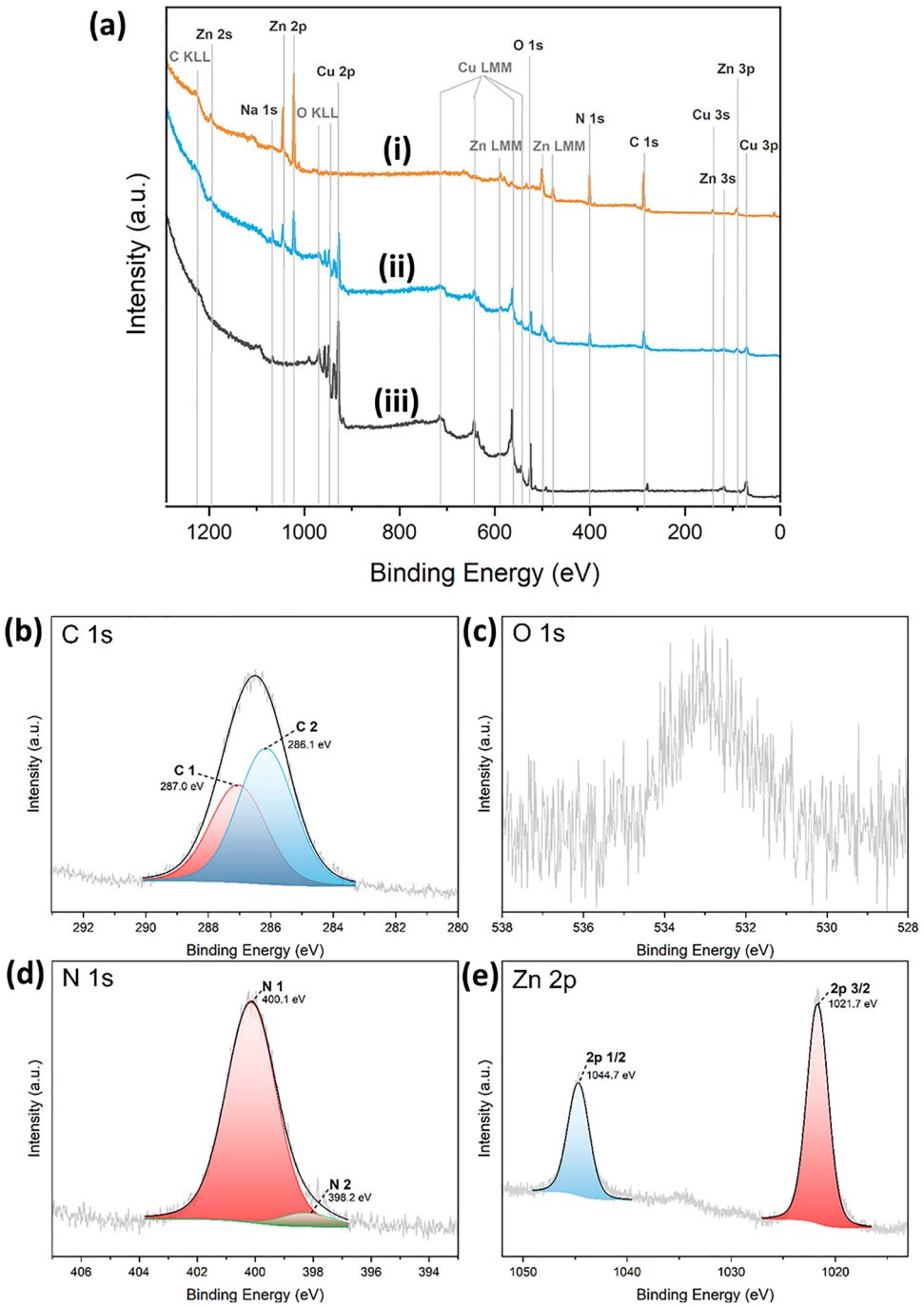

Fig. 5 XPS spectra of selected CuO:Al samples: (a) labelled survey spectra of: (i) ZIF-8/CuO:Al (high coverage), the spectrum shows the ZIF-8 characteristic XPS lines of Zn, N and C indicating complete coverage of the substrate. (ii) ZIF-8/CuO:Al (low coverage), the Cu specific substrate lines are still visible, and (iii) CuO:Al reference sample. (b)–(e) High-resolution spectra of the ZIF-8/CuO:Al (high coverage) sample: (b) C 1s, (c) O 1s, (d) N 1s, and (e) Zn 2p.

spectrum with Zn $2p_{3/2}$ and Zn $2p_{1/2}$ lines at 1021.7 and 1044.7 eV. The binding energies and the difference between these two lines of approximately 23 eV are consistent with Zn in the +2-oxidation state present in the ZIF-8, as confirmed in the corresponding literature.[58,75] The presented XPS results which match with ZIF-8 specific literature as well as the assignments of the C 1s peak strongly indicate that the ZIF-8/CuO:Al (high coverage) sample possesses an intact ZIF-8 layer on the CuO:Al surface.

Fig. S5(a)–(d) shows the XPS high resolution spectra of the ZIF-8/CuO:Al (low coverage) sample. Here, a differential charging effect can be observed which complicates a thorough analysis. Nevertheless, the ZIF-8 specific N 1s (Fig. S5(c)) and Zn 2p (Fig. S5(d)) spectra closely align with the corresponding

spectra of the ZIF-8/CuO:Al (high coverage) sample, indicating that an intact ZIF-8 is also present on the surface of the ZIF-8/CuO:Al (low coverage) sample.

In addition to these spectra interpretations, the XPS composition analysis of the ZIF-8/CuO:Al (high coverage) was calculated to be approximately 56.2 at% C, 25.5 at% N, 16.3 at% Zn, as well as 2.0 at% oxygen. These values are compatible with values found for ZIF-8 in the literature.[74] Note, that the exact chemical composition and the resulting XPS spectra can be slightly influenced by the preparation method employed for the synthesis and deposition of ZIF-8.

N_2 adsorption–desorption isotherm was measured at 77 K to analyze the surface area of ZIF-8 nanoparticles. Fig. S6 presents the corresponding graph. The isotherm exhibits type-I behavior, indicating a microporous structure. BET (Brunauer–Emmett–Teller) surface area is calculated to be 1647 $m^2 g^{-1}$, which is in good agreement with reported values.[76]

Gas sensing investigations

The gas sensing performance of the CuO:Al film-based sensor was evaluated against a series of gases- hydrogen, *n*-butanol, 2-propanol, ethanol, acetone, and ammonia- at different operating temperatures (OPTs) ranging from room temperature to 350 °C. No measurable response from these sample sets was observed at temperatures below 250 °C. At 300 °C, the sensor exhibited gas responses of 84% for hydrogen, 80% for 2-propanol, and 54% for *n*-butanol. At 350 °C, the corresponding responses were 90% for hydrogen, 70% for 2-propanol, and 60% for *n*-butanol. These results indicate that the selectivity between *n*-butanol and 2-propanol is more pronounced at 300 °C than at 350 °C, as shown in Fig. 6(a). Fig. 6(b) illustrates the dynamic characteristics to 100 ppm hydrogen over three cycles at OPT of 350 °C. Baseline drift observed in the hydrogen response (Fig. 6(b) and (c)) could be attributed to reaction product residues on the sensing surface.[77] The response/recovery time for hydrogen was observed as 17.1 s/37.1 s at 350 °C. The associated error in the response and recovery times is ±0.5 s. Fig. 6(c) presents the dynamic response to 100 ppm tested gases at 350 °C. The highest gas sensing response as discussed above was observed for hydrogen (~90%), followed by 2-propanol (~70%) and *n*-butanol (~60%). Fig. 6(d) displays the current–voltage (*I*–*V*) characteristics of the CuO:Al film, revealing typical Ohmic behavior. As the temperature increases from room temperature to 350 °C, thermal excitation leads to an increase in electrical charge carriers within the semiconductor-based sensor, resulting in an increased sensor current.[78] However, at 350 °C, a deviation from linearity emerges in the *I*–*V* characteristics at lower and higher end of voltages, confirmed by the reported study.[79]

Fig. 7(a) illustrates the gas sensing response of the ZIF-8/CuO:Al sensor to 100 ppm of hydrogen, *n*-butanol, 2-propanol,

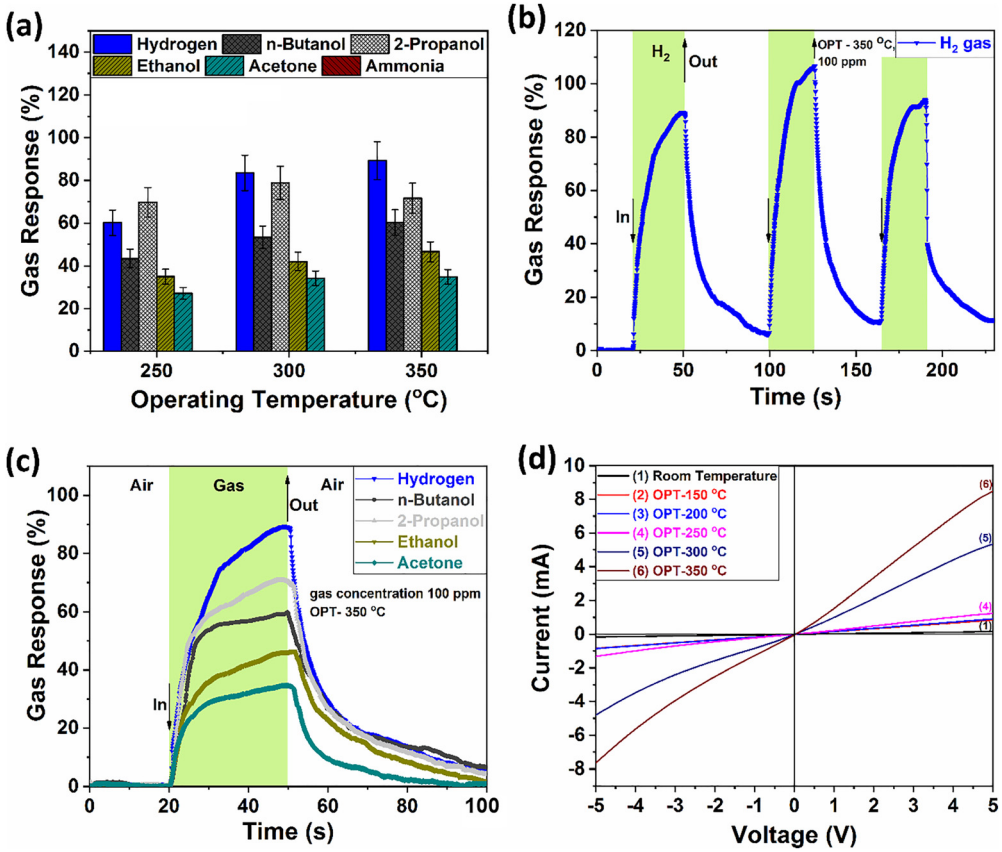

Fig. 6 Gas response of the CuO:Al film-based sensor: (a) to a series of gases with concentration of 100 ppm at 350 °C, (b) dynamic response to 100 ppm of hydrogen gas at 350 °C, and (c) dynamic characteristic of all the tested gases at 350 °C; (d) current–voltage (*I*–*V*) characteristics at different OPTs.

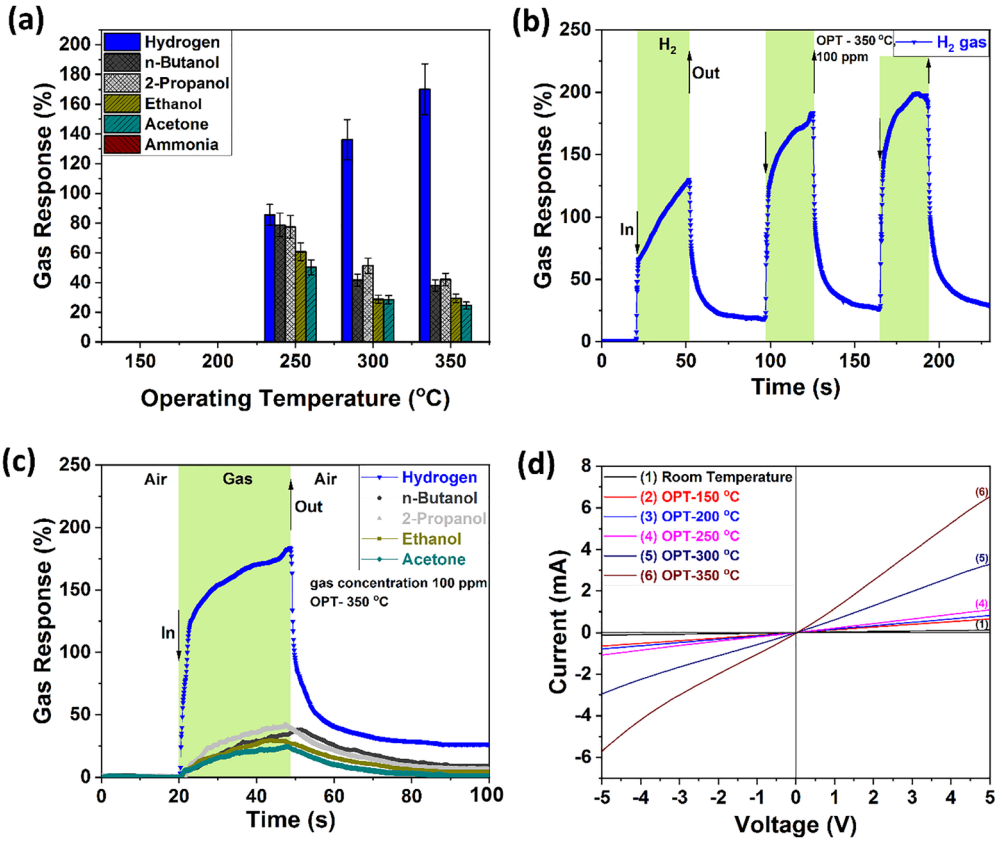

Fig. 7 Gas response of the ZIF-8/CuO:Al based sensor: (a) to a series of gases with a concentration of 100 ppm, (b) dynamic response to hydrogen at 350 °C, (c) dynamic characteristic of all the tested gases at 350 °C; and (d) current–voltage (*I*–*V*) characteristics at different OPTs.

ethanol, acetone, and ammonia, at different operating temperatures (OPTs) ranged from 150 °C to 350 °C. The OPT significantly influences gas sensing by affecting the electrical conductivity and electrical charge mobility of the sensing material. At lower OPTs (150 °C, 200 °C), no discernible gas response was observed, likely due to factors such as slow reaction kinetics and insufficient thermal energy to overcome the activation energy barrier for the reaction of analyte with the sensor surface.[80] As the temperature increases from 250 °C to 350 °C, the hydrogen response increases, reaching the maximum of 170% at 350 °C. Conversely, the responses to other gases exhibited a bell-shaped curve, with a maximum at 250 °C, followed by a decrease likely due to faster desorption at higher temperatures.[81] Notably, among the ABE gases, *n*-butanol exhibited the highest response across all the OPTs, indicating a stronger affinity compared to acetone and ethanol. This observation is supported by competitive adsorption isotherms in ternary ABE systems.[82] The fabricated sensor shows ~1.3 and ~1.6 times higher selectivity to *n*-butanol as compared to ethanol and acetone, respectively. The sensing response to hydrogen gas at 350 °C exceeded that of the other tested gases by a factor of >4. Fig. 7(b) demonstrates the dynamic response to 100 ppm hydrogen over three cycles at 350 °C. The corresponding response and recovery times for hydrogen were observed to be 11.1 s and 27.0 s, respectively, with an associated error of ±0.5 s. Fig. 7(c) shows the dynamic response to 100 ppm of each gas at OPT of 350 °C. The increased hydrogen gas response may be due to enhanced diffusion at higher temperatures. Baseline drift observed in the hydrogen gas response (Fig. 7(b) and (c)) could be attributed to reaction product residues on the sensing surface, as described in eqn (5)–(7).[77]

$$H_2 + 2CuO \rightarrow H_2O + Cu_2O \quad (5)$$

$$H_2 + Cu_2O \rightarrow H_2O + 2Cu \quad (6)$$

$$H_2 + CuO \rightarrow H_2O + Cu \quad (7)$$

Part of the H_2O molecules produced according to the Equations above may strongly bond to active sites of the CuO forming hydroxyl adsorbed species, which can retard hydrogen desorption completely and lead to a baseline drift in subsequent cycles,[83] as shown in Fig. 7(b). A slight increase in sensing response in subsequent cycles may be attributed to the annealing history (*i.e.*, repetitive high-temperature measurements), as reported in the literature.[84]

Fig. 7(d) shows the current–voltage (*I*–*V*) characteristics of the MOF ZIF-8/CuO:Al hybrid sensor exhibiting typical Ohmic behavior. As the temperature increases from room temperature to 350 °C, the thermal excitation causes the increase of carriers in the semiconductor sensor, resulting in an increased current.[78] However, at OPT of 350 °C, a deviation from linearity

emerges in the *I–V* characteristics at lower and higher end of voltages, confirmed by the reported study.[79] CuO is a p-type semiconductor-oxide material. At constant OPT, the electrical resistance of the gas sensor depends on the amount of O_2 adsorbed on the sensing surface.[19]

A comparative visualization of the gas sensing responses of the MOF ZIF-8/CuO:Al and CuO:Al sensors to the tested gases (hydrogen, *n*-butanol, 2-propanol, ethanol, acetone, and ammonia), based on data from Fig. 6 and 7, is presented in Fig. S7. Prior to ZIF-8 deposition on the CuO:Al film, the sensor exhibited ∼1.5 times higher selectivity for hydrogen compared to *n*-butanol at 350 °C. After MOF ZIF-8 deposition, the ZIF-8/CuO:Al hybrid sensor demonstrated more than a four-fold increase in selectivity for hydrogen over *n*-butanol. The enhanced selectivity for hydrogen over other analytes, as discussed above, can be attributed to the molecular sieving effect of ZIF-8, which preferentially permits smaller hydrogen molecules (2.89 Å)[47] to diffuse through its pores and reach the CuO:Al surface.

The working temperature affects the gas sensor's performance. Fig. S7 shows the sensing performance of the CuO:Al and MOF ZIF-8/CuO:Al films as a function of OPT for 100 ppm of various tested gases in our experiments. In case of the CuO:Al film without ZIF-8 coating, no appreciable variation in response was observed for tested ABE molecules at different OPTs. For the ZIF-8/CuO:Al film-based structure, the sensing response to ABE molecules initially increases as the temperature rises from 150 °C to 250 °C, followed by a decline when the temperature is further increased to 350 °C. This can be attributed to the thermal effect influencing the adsorption–desorption process of ABE molecules on the adsorbent surface.[85] Thus, among the tested temperatures, 250 °C appears to be the most favourable temperature for ABE molecules sensing using the MOF ZIF-8/CuO:Al sensor. The enhancement in the sensing response after metal–organic framework ZIF-8 coating on the CuO:Al surface can be attributed to the accumulation of tested analyte due to high porosity and ZIF-8 also serves as a concentrator for the analyte.[86]

To study the location of the defect states above the valence band, the activation energy (E_a) of the ZIF-8/CuO:Al sample was assessed by measuring current (I) in ambient environment at different temperatures ranging from room temperature (25 °C) to 350 °C. By plotting ln (I) *versus* $1/T$ (Fig. 8), the slope of the linear fit can be determined, which corresponds to the activation energy (E_a) divided by the Boltzmann constant (k_B) according to the Arrhenius equation:[15]

$$\text{Slope} = -\frac{E_a}{k_B} \tag{8}$$

The slope of the plotted curve is -2.4×10^3 K. Thus, the activation energy from the valence band to the defect state is approximately ∼0.2 eV. This activation energy is corresponding to the trap levels or defect states (V_{Cu}).[87–89] These trap levels act as acceptor states and are primarily responsible for CuO's p-type conductivity. These shallow trap levels just above the valence band enables the thermal excitation of electrons from the valence band into the acceptor level, thereby creating holes in the valence band that contribute to hole conduction.

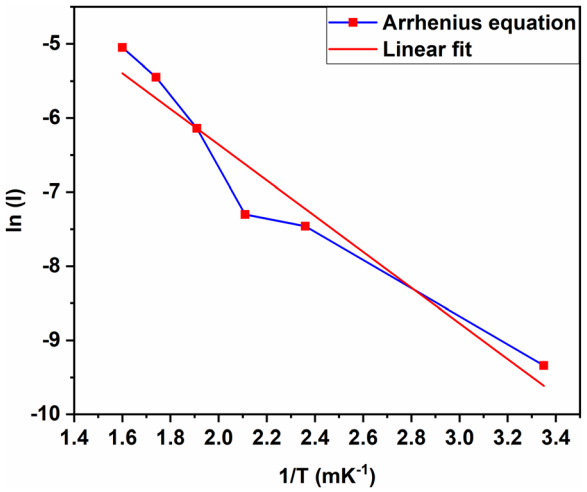

Fig. 8 Arrhenius plot of ln (I) *vs.* $1/T$ with the corresponding linear fit for the calculation of activation energy of the ZIF-8/CuO:Al sample.

Fig. 9(a) illustrates the gas response of the ZIF-8/CuO:Al film-based structure to varying hydrogen gas concentrations between 10 to 1000 ppm under operating conditions of RH 11% at OPT of 350 °C. The sensor detects hydrogen gas at a concentration as low as 10 ppm, with a response of ∼50%. As the hydrogen gas concentration increases, the response also increases, reaching ∼400% at 1000 ppm.

Similarly, at RH 50%, Fig. 9(b) shows the gas response of the ZIF-8/CuO:Al film-based sensor to hydrogen gas concentrations ranging from 10 to 1000 ppm. Notably, the response at 10 ppm is nearly identical at both humidity levels. However, differences are observed at 100 and 1000 ppm. Increasing the RH from 11% to 50% results in no significant deterioration of the hydrogen gas sensing response. The response decreases only from ∼170% to ∼152% by increasing the RH from 11% to 50% at a concentration of 100 ppm. This minimal change can be attributed to the hydrophobic properties of the ZIF-8 layer on CuO:Al.[90] Moreover, the gas sensing response decreases to approximately 75% at a concentration of 100 ppm with a further increase in RH to 81%, as illustrated in Fig. S8.

The theoretical value of lowest detection limit (LDL) of the sensor is defined as the smallest concentration of an analyte that can be reliably detected. According to the International Union of Pure and Applied Chemistry (IUPAC) definition, it is the smallest distinguishable signal from the noise that can be detected by a tested sensor after the exposure to the lowest amount of tested analyte.[91] It is a crucial parameter in evaluating the sensing performance and can be expressed in parts per million (ppm) or parts per billion (ppb). Fig. 10 shows the gas sensing response (S) as a function of hydrogen concentration. LDL and root mean square noise (rms_{noise}) are defined in eqn (9) and (10), respectively.

The LDL can be expressed in mathematical form as:[92]

$$\text{LDL} = \frac{3 \times \text{rms}_{\text{noise}}}{g} \tag{9}$$

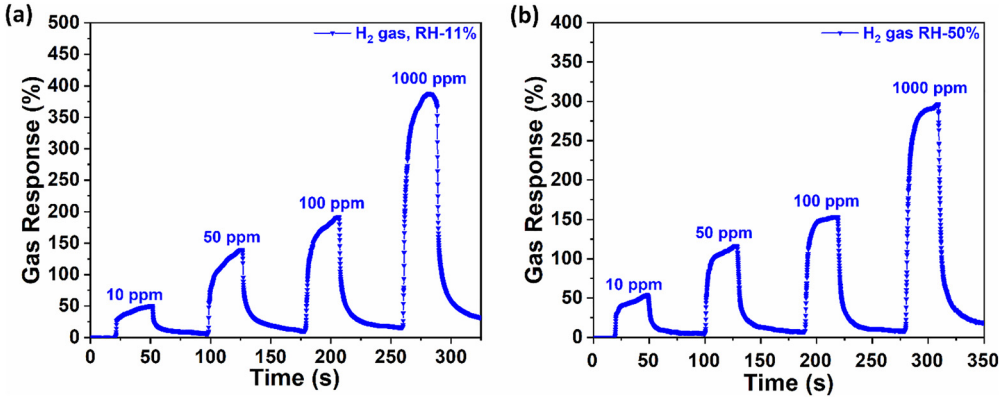

Fig. 9 Gas response of the ZIF-8/CuO:Al based hybrid sensor to different hydrogen concentrations and RH values (a) RH 11%, and (b). RH 50%.

and rms_{noise} can be expressed as:[93]

$$rms_{noise} = \sqrt{\frac{\sum_i (R_i - R)^2}{n}} \quad (10)$$

where g is the slope of the linear fitting of sensing response (%) to the concentration of the analyte (ppm) calculated through linear fitting at the low concentration (up to 100 ppm), R_i's are the experimental data points of the baseline before gas exposure, R is the average value of the baseline consecutive data points before gas exposure, and n is the number of data points on the baseline before gas exposure.

The calculated value of rms_{noise} is 0.18% and the slope (g) of the sensing response as a function of the analyte concentration is 1.34% ppm. Thus, the value of LDL of the ZIF-8/CuO:Al based gas sensor is ~402 ppb.

To check the temporal stability of the ZIF-8/CuO:Al film-based hybrid sensor, the dynamic response for different concentrations of hydrogen gas was measured at RH 11% and RH 50% after three and four weeks, respectively.

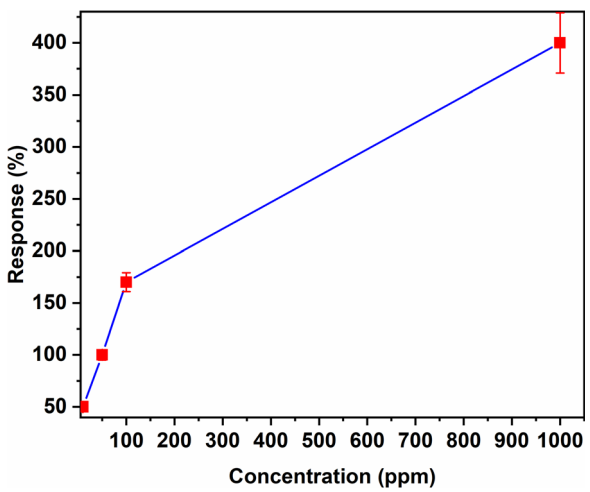

Fig. 10 Sensing response (%) of the ZIF-8/CuO:Al film-based sensor as a function of the hydrogen concentration (ppm).

Fig. 11 and 12 demonstrate the dynamic gas sensing response to hydrogen gas concentrations ranging from 10 to 1000 ppm measured three and four weeks after initial testing, respectively. These figures reveal that the response decreases slightly under higher humidity conditions (RH 50%) compared to less humid environments (RH 11%), especially for higher hydrogen gas concentrations. However, the sensor maintains consistent response values at 10 ppm hydrogen concentrations across both humidity levels and time periods-retaining its detection efficiency even after four weeks. This demonstrates exceptional temporal stability of the fabricated sensor.

A comparative study with previously reported literature is presented in Table S1. Our current study demonstrates good temporal stability, maintaining performance over four weeks, and achieves a low detection limit of 402 ppb. Defect analysis, derived from the Arrhenius equation (~0.2 eV, V_{Cu}), provides insights into the material's electronic properties. Additionally, the sensor exhibits strong sensitivity retention even under high RH conditions (RH 50%), highlighting its robustness for real-world applications.

Gas sensing mechanism

CuO is a typical p-type semiconductor due to the presence of copper interstitial defects that lead to the formation of an acceptor state just above the valence band, as shown in Fig. S9. When the sensor is exposed to the ambient atmosphere, adsorbed oxygen molecules on the sensor surface are ionized to different oxygen ionic species depending on the OPT, as shown in eqn (11)–(14).[94]

$$O_{2(gas)} \leftrightarrow O_{2(ads.)} \quad (11)$$

$$O_{2(ads.)} \leftrightarrow O^-_{2(ads.)} + h^+ \quad (12)$$

$$O^-_{2(ads.)} \leftrightarrow 2O^-_{(ads.)} + h^+ \quad (13)$$

$$O_{2(ads.)} \leftrightarrow O^{2-}_{(ads.)} + h^+ \quad (14)$$

$$H_2 + O^-_{(ads.)} + h^+ \rightarrow H_2O_{(vap.)} \quad (15)$$

$$C_4H_9OH_{(ads.)} + 12O^-_{(ads.)} + 12h^+ \rightarrow 4CO_2 + 5H_2O \quad (16)$$

Different oxygen ionic species are adsorbed on the surface. As shown in eqn (12), the molecular oxygen ionic species (O_2^-)

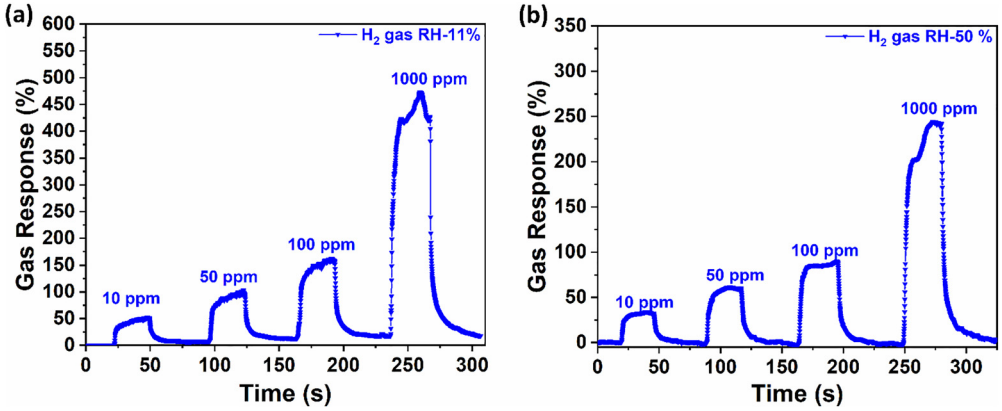

Fig. 11 Gas response of the ZIF-8/CuO:Al based hybrid sensor to different hydrogen gas concentrations and RH values (a) RH 11%, and (b) RH 50% after three weeks.

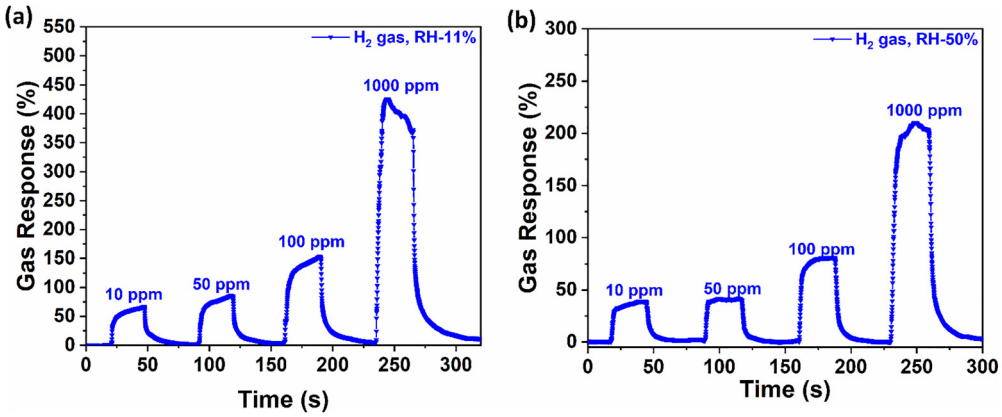

Fig. 12 Gas response of the ZIF-8/CuO:Al based hybrid sensor to different hydrogen gas concentrations and RH values (a) RH 11%, and (b) RH 50% after four weeks.

forms at temperature below 100 °C. Eqn (13) and (14) show the origin of monoionic oxygen (O^-) and bionic oxygen (O^{2-}) species occurring in the temperature range 100 °C < T < 300 °C and above 300 °C, respectively. Holes (h^+) are generated due to the transfer of electrons to the surface acceptor level just above the valence band as shown in Fig. S9. After exposure to the reducing gas hydrogen (H_2), the reduction of the hole accumulation layer (HAL) occurs on the surface of CuO:Al, as shown in eqn (15).[95] Similarly, after exposure to *n*-butanol (C_4H_9OH) on the CuO:Al surface, the HAL width decreases due to hole reduction, as shown in eqn (16).[19] The adsorption and desorption of target gases, along with their interaction with adsorbed oxygen ionic species, modulate the electrical resistance and thereby, producing the sensing response. The energy band representation of the ZIF-8/CuO:Al film after exposure to hydrogen and *n*-butanol is shown in Fig. S9. The gas sensing mechanism of the chemoresistive ZIF-8/CuO:Al hybrid sensor film can be correlated to adsorption of hydrogen and other gases onto the sensing surface. The ZIF-8 coating enhances the adsorption capacity due to its highly porous structure, which facilitates the diffusion of hydrogen through the coating and its interaction with the CuO:Al sensing surface.[96] The change in electronic properties of the CuO:Al surface occurs after hydrogen adsorption on hollow sites of Cu atoms. The cleavage of H–H bond, followed by the formation of two O–H bonds may need more energy due to the high oxygen vacancy concentration, making the reaction between hydrogen and CuO more difficult to proceed.[97] Eqn (7)[98] shows the reaction between CuO and hydrogen molecule.

Using standard kinetic theory of gas molecules, the mean free path can be calculated using the relation:[99]

$$\lambda = \frac{k_B T}{\sqrt{2}\pi d_{ij}^2 p} \quad (17)$$

where λ is the mean free path of gas molecules, T is the operating temperature, d_{ij} is the collision diameter, and p is the atmospheric pressure.

Since the target gas molecules (*e.g.* 100 ppm) are very low in concentration compared to the background gas. Number density of background gas molecules dominate. So, λ is independent of small mole fraction and atmospheric pressure is considered in eqn (17).

At 350 °C, the mean free path for all the test gases (hydrogen, acetone, 2-propanol, *n*-butanol, and ethanol) can be calculated and comes out to be (164.9 nm, 94.5 nm, 94.2 nm, 75.7 nm, and 115 nm, respectively).

The flow regime of the transport of gas molecules can be classified in three classes based on their Knudsen number (K_n), which can be defined as:[99]

$$K_n = \frac{\lambda}{s_p} \quad (18)$$

where s_p (0.34 nm)[46] is the pore size of the ZIF-8 nanoparticle.

At 350 °C, the Knudsen number for all the test gases can be calculated using eqn (18). In each case, the Knudsen number is found to be greater than 10, which indicates that gas transport occurs in the Knudsen diffusion regime. For instance, the Knudsen numbers at 350 °C for hydrogen and *n*-butanol are approximately 485 and 223, respectively.

If all the target gas molecules were to pass exclusively through the intrinsic ZIF-8 pores, diffusion would proceed *via* Knudsen diffusion. Moreover, SEM analysis shows that the CuO:Al film is completely covered by the ZIF-8 layer. However, the MOF ZIF-8 film is not perfectly pinhole-free: grain boundaries and other small defects may be present. These structural imperfections can locally increase the effective pore size, allowing for contribution from translational or even molecular diffusion in some regions. Therefore, it can be concluded that while Knudsen diffusion is the dominant transport mechanism through the intrinsic ZIF-8 pores, translational or molecular diffusion may also contribute locally at grain boundaries and defects.

Fig. S9 shows the schematic diagram of hydrogen (2.89 Å)[47] sensing through ZIF-8 layer due to its smaller kinetic diameter over other tested VOCs such as ethanol (4.53 Å),[47] 2-propanol (4.7 Å),[100] *n*-butanol (5.0 Å),[101] and acetone (4.6 Å).[47] Although the nominal aperture size of ZIF-8 pore is 3.4 Å,[46] it is not sharp molecular sieving cut-off due to its flexible framework.[46] The large pore size of ZIF-8 (11.6 Å)[46] have been shown to be accessible to a series of VOC molecules with kinetic diameters of 4.3–5.85 Å, which is significantly larger than the nominal aperture size of ZIF-8.[46] The interaction of VOC molecules with ZIF-8 may depend on the electronic polarizability and their van-der Waals interaction with the ZIF-8 framework. The electronic polarizability of *n*-butanol (~8.57)[102] is highest followed by 2-propanol (~6.67),[102] acetone (~6.27),[102] and ethanol (~4.92),[102] which leads to have higher adsorption of *n*-butanol on ZIF-8 due to its strong van der Waals interaction with the ZIF-8 framework. Based on Remi *et al.* report, the liquid-phase adsorption profiles of VOCs on ZIF-8 were examined at room temperature, which shows largest uptake of *n*-butanol followed by 2-propanol, acetone, and ethanol, respectively.[103,104] In the current study, the diffused molecules through ZIF-8 interacts at the CuO:Al sensing surface. We have observed a bell-shaped curve with the highest sensing response for VOCs at 250 °C, followed by a decrease at higher temperatures due to the dominance of desorption. At 250 °C, the gas sensing responses of *n*-butanol and 2-propanol are almost equal within the error margin, with *n*-butanol showing a slightly higher response.

Conclusions

In this study, CuO:Al thin films were synthesized using an SCS method. Metal–organic frameworks ZIF-8 nanoparticles were applied onto the synthesized CuO:Al films by drop-casting a nanoparticle dispersion. XRD analysis confirmed the crystallographic structure of the ZIF-8/CuO:Al film-based structure, verifying the presence of monoclinic phase of CuO. The crystallite size of the ZIF-8 nanoparticles was estimated to be approximately 30 nm using the Scherrer Equation, indicating the coherent diffraction domain size. SEM provided detailed insights into the surface morphology, revealing highly dense triangular-shaped CuO:Al grains and a uniform distribution of rhombic dodecahedral ZIF-8 nanoparticles on the CuO:Al film. The particle size of ZIF-8 was estimated to be about 70 nm based on SEM images. EDX provided compositional information, confirming the presence of aluminium at 0.2 at%, which was not detected by XRD. TGA indicated that the metal–organic frameworks ZIF-8 remains thermally stable up to approximately 380 °C. XPS gives detailed insight about the chemical states and elemental composition of the film, confirming the integrity of the ZIF-8 layer after deposition on the CuO:Al film. The N_2-adsorption isotherm analysis determined a BET surface area of ~1647 m^2 g^{-1} and exhibited type-I isotherm behavior, characteristic of ZIF-8. Additionally, Raman spectroscopy supports the structural analysis by identifying vibrational modes corresponding to the ZIF-8 and CuO phases. ZIF-8/CuO:Al-based hybrid sensor retains its hydrogen detection efficiency at RH 11% and RH 50% even after four weeks following the initial measurements. ZIF-8/CuO:Al film-based sensor demonstrates exceptional sensing performance in terms of temporal stability, sensing response at low concentration (10 ppm) and durability even in the presence of higher RH (81%). The current measurements at different operating temperatures reveal information about the location of defect states by calculating activation energy of the sensor. Considerably, the fabricated sensor exhibits appreciable selectivity to hydrogen (>4 times) over other tested analytes such as acetone, 2-propanol, *n*-butanol, and ethanol at higher temperature (350 °C). The fabricated hybrid sensor shows ~1.3 and ~1.6 times higher selectivity to *n*-butanol as compared to ethanol and acetone, respectively. The ZIF-8/CuO:Al-based hybrid sensor exhibited appreciable sensitivity (75%) for 100 ppm hydrogen gas even at a high relative humidity of 81%, enabling its application under adverse conditions. Furthermore, a very low detection limit of 402 ppb was achieved, which is advantageous for various applications, including the detection of very small amount of hydrogen leaks. These remarkable features make the metal–organic frameworks ZIF-8/CuO:Al film-based hybrid sensor developed in current work, a highly promising candidate for efficient hydrogen sensing under different environmental conditions.

Author contributions

Rajat Nagpal: conceptualization, data curation, formal analysis, investigation, methodology, software, validation, visualization,

writing – original draft, writing review and editing; Masaya Sugihara: data curation, formal analysis, investigation, validation, writing review and editing; Nicolae Magariu: formal analysis, investigation, visualization; Tim Tjardts: visualization, writing review and editing; Nahomy Meling: investigation, visualization; Thomas Strunskus: formal analysis, investigation, visualization, writing review and editing; Tayebeh Ameri: resources, supervision; Rob Ameloot: funding acquisition, project administration, resources, supervision; Rainer Adelung: funding acquisition, project administration, resources, supervision; Oleg Lupan: conceptualization, funding acquisition, project administration, resources, supervision, validation, writing review and editing.

Conflicts of interest

There are no conflicts to declare.

Data availability

The data supporting this article have been included in the article and supplementary information (SI). The associated content in the supplementary information contains SEM images of the CuO:Al film at different magnifications. SEM images of CuO:Al film on glass substrate and ZIF-8 nanoparticles on Si substrate showing the particle size. The SEM image of the investigated area of the CuO:Al film and the composition images using EDX mapping. TGA profile for ZIF-8 weight decomposition in the synthetic air. High-resolution XPS spectra of the ZIF-8/CuO:Al (low coverage) sample. Nitrogen adsorption–desorption isotherm curve of the ZIF-8 nanoparticles. The comparative visualization of the gas responses of the ZIF-8/CuO:Al and CuO:Al sensors to a series of gases with concentration 100 ppm at different operating temperatures. The effect of operating temperature on the gas sensing response of the ZIF-8 coated CuO:Al film at the relative humidity (RH) of 81%. Schematic diagram illustrating the gas sensing mechanism of the CuO:Al film. Comparative study with the reported literature in tabular form. See DOI: **https://doi.org/10.1039/d5qm00565e**.

Acknowledgements

This project has received funding from the European Union's EU Framework Programme for Research and Innovation Horizon Europe under grant agreement no 101072845. We would like to thank Dr. Haoyi Qiu for his assistance in performing the micro-Raman spectroscopy measurements in this study. This research was partially supported by the State Program 020401, LIFETECH No. 020404 at the Technical University of Moldova. T. A. acknowledges finance support of DFG Heisenberg Programme, project AM 519/4-1.

References

1 I. Mcfarlane, L. Alyanak, J. Jensen, R. Kollodge, J. Daldin, T. Jayaram, L. Ratcliffe, C. Trautwein, D. Baker, N. Botev, A. Garbett, S. Gietel-Basten, G. Luchsinger, R. Nandagiri, R. Sear, T. Sobotka, A. Armitage, S. Chalasani, J.-H. Eschenbaecher, M. Herrmann, S. Simelane and R. Snow, Infinite possibilities the case for rights and choices State of World, *Population report*, 2023, 1–192.

2 J. Baeyens, Waste Energy Harvesting: Mechanical and Thermal Energies. By Ling Bing Kong, Tao Li, Huey Hoon Hng, Freddy Boey, Tianshu Zhang, and Sean Li, *Energy Technol.*, 2015, **3**, 790.

3 A. Velazquez Abad and P. E. Dodds, Green hydrogen characterisation initiatives: Definitions, standards, guarantees of origin, and challenges, *Energy Policy*, 2020, **138**, 111300.

4 Z. Chen, Z. Wu, J. Liu and C. Lee, Combustion and emissions characteristics of high *n*-butanol/diesel ratio blend in a heavy-duty diesel engine and EGR impact, *Energy Convers. Manage.*, 2014, **78**, 787–795.

5 S. Jung, H. Kim, Y. F. Tsang, K.-Y. A. Lin, Y.-K. Park and E. E. Kwon, A new biorefinery platform for producing (C2-5) bioalcohols through the biological/chemical hybridization process, *Bioresour. Technol.*, 2020, **311**, 123568.

6 Y.-C. Chang, W.-J. Lee, T. S. Wu, C.-Y. Wu and S.-J. Chen, Use of water containing acetone–butanol–ethanol for NOx-PM (nitrogen oxide-particulate matter) trade-off in the diesel engine fueled with biodiesel, *Energy*, 2014, **64**, 678–687.

7 R. Thayil and S. R. Parne, Molybdenum ditelluride nanostructures for enhanced room temperature *n*-butanol detection, *J. Mater. Sci.: Mater. Electron.*, 2024, **35**, 1515.

8 B. Han, X. Liu, X. Xing, N. Chen, X. Xiao, S. Liu and Y. Wang, A high response butanol gas sensor based on ZnO hollow spheres, *Sens. Actuators, B*, 2016, **237**, 423–430.

9 A. M. Sadeq, R. Z. Homod, A. K. Hussein, H. Togun, A. Mahmoodi, H. F. Isleem, A. R. Patil and A. H. Moghaddam, Hydrogen energy systems: Technologies, trends, and future prospects, *Sci. Total Environ.*, 2024, **939**, 173622.

10 F. Ferrada, F. Babonneau, T. Homem-de-Mello and F. Jalil-Vega, The role of hydrogen for deep decarbonization of energy systems: A Chilean case study, *Energy Policy*, 2023, **177**, 113536.

11 S. Griffiths, B. K. Sovacool, J. Kim, M. Bazilian and J. M. Uratani, Industrial decarbonization via hydrogen: A critical and systematic review of developments, socio-technical systems and policy options, *Energy Res. Soc. Sci.*, 2021, **80**, 102208.

12 M. Rüdisüli, S. L. Teske and U. Elber, Impacts of an Increased Substitution of Fossil Energy Carriers with Electricity-Based Technologies on the Swiss Electricity System, *Energies*, 2019, **12**, 2399, DOI: **10.3390/en12122399**.

13 V. S. Bhati, M. Hojamberdiev and M. Kumar, Enhanced sensing performance of ZnO nanostructures-based gas sensors: A review, *Energy Rep.*, 2020, **6**, 46–62.

14 S. B, A. John and P. K. Panda, A review on metal-oxide based p–n and n–n heterostructured nano-materials for gas sensing applications, *Sens. Int.*, 2021, **2**, 100085.

15 R. Nagpal, C. Lupan, A. Buzdugan, V. Ghenea and O. Lupan, Effect of Pd functionalization on optical and

hydrogen sensing properties of ZnO:Eu films, *Optik*, 2025, **325**, 172247, DOI: 10.1016/j.ijleo.2025.172247.

16 F. Moosavi, M. E. Bahrololoom, R. Kamjou, A. Mirzaei, S. G. Leonardi and G. Neri, Hydrogen Sensing Properties of Co-Doped ZnO Nanoparticles, *Chemosensors*, 2018, **6**(4), 61, DOI: 10.3390/chemosensors6040061.

17 S. K. Biswas and P. Pramanik, Studies on the gas sensing behaviour of nanosized $CuNb_2O_6$ towards ammonia, hydrogen and liquefied petroleum gas, *Sens. Actuators, B*, 2008, **133**, 449–455.

18 Z. Zhao, M. Knight, S. Kumar, E. T. Eisenbraun and M. A. Carpenter, Humidity effects on Pd/Au-based all-optical hydrogen sensors, *Sens. Actuators, B*, 2008, **129**, 726–733.

19 R. Nagpal, C. Lupan, A. Bîrnaz, A. Sereacov, E. Greve, M. Gronenberg, L. Siebert, R. Adelung and O. Lupan, Multifunctional Three-in-One Sensor on t-ZnO for Ultraviolet and VOC Sensing for Bioengineering Applications, *Biosensors*, 2024, **14**(6), 293, DOI: 10.3390/bios14060293.

20 L. Siebert, N. Wolff, N. Ababii, M.-I. Terasa, O. Lupan, A. Vahl, V. Duppel, H. Qiu, M. Tienken, M. Mirabelli, V. Sontea, F. Faupel, L. Kienle and R. Adelung, Facile fabrication of semiconducting oxide nanostructures by direct ink writing of readily available metal microparticles and their application as low power acetone gas sensors, *Nano Energy*, 2020, **70**, 104420, DOI: 10.1016/j.nanoen.2019.104420.

21 O. Lupan, V. Postica, V. Cretu, N. Wolff, V. Duppel, L. Kienle and R. Adelung, Single and networked CuO nanowires for highly sensitive p-type semiconductor gas sensor applications, *Phys. Status Solidi RRL*, 2016, **10**, 260–266, DOI: 10.1002/pssr.201510414.

22 X. Li, Y. Wang, Y. Lei and Z. Gu, Highly sensitive H_2S sensor based on template-synthesized CuO nanowires, *RSC Adv.*, 2012, **2**, 2302–2307.

23 A. Živković and N. H. de Leeuw, Exploring the formation of intrinsic p-type and n-type defects in CuO, *Phys. Rev. Mater.*, 2020, **4**, 74606.

24 Q. Zhang, D. Xu, X. Zhou, X. Wu and K. Zhang, In Situ Synthesis of CuO and Cu Nanostructures with Promising Electrochemical and Wettability Properties, *Small*, 2014, **10**, 935–943.

25 S. P. Selvaraj, Enhanced surface morphology of copper oxide (CuO) nanoparticles and its antibacterial activities, *Mater. Today: Proc.*, 2022, **50**, 2865–2868.

26 I. Kumar, P. Ranjan and A. R. Quaff, Cost-effective synthesis and characterization of CuO NPs as a nanosize adsorbent for As(III) remediation in synthetic arsenic-contaminated water, *J. Environ. Health Sci. Eng.*, 2020, **18**, 1131–1140.

27 S. Ali, A. Razzaq, H. Kim and S.-I. In, Activity, selectivity, and stability of earth-abundant $CuO/Cu_2O/Cu0$-based photocatalysts toward CO_2 reduction, *Chem. Eng. J.*, 2022, **429**, 131579.

28 H.-J. Kim and J.-H. Lee, Highly sensitive and selective gas sensors using p-type oxide semiconductors: Overview, *Sens. Actuators, B*, 2014, **192**, 607–627.

29 F. Wang, H. Li, Z. Yuan, Y. Sun, F. Chang, H. Deng, L. Xie and H. Li, A highly sensitive gas sensor based on CuO nanoparticles synthetized *via* a sol–gel method, *RSC Adv.*, 2016, **6**, 79343–79349.

30 L.-J. Zhou, Y.-C. Zou, J. Zhao, P.-P. Wang, L.-L. Feng, L.-W. Sun, D.-J. Wang and G.-D. Li, Facile synthesis of highly stable and porous Cu_2O/CuO cubes with enhanced gas sensing properties, *Sens. Actuators, B*, 2013, **188**, 533–539.

31 N. D. Hoa, N. Van Quy, H. Jung, D. Kim, H. Kim and S. K. Hong, Synthesis of porous CuO nanowires and its application to hydrogen detection, *Sens. Actuators, B*, 2010, **146**, 266–272.

32 O. Lupan, D. Santos-Carballal, N. Ababii, N. Magariu, S. Hansen, A. Vahl, L. Zimoch, M. Hoppe, T. Pauporté, V. Galstyan, V. Sontea, L. Chow, F. Faupel, R. Adelung, N. H. de Leeuw and E. Comini, $TiO_2/Cu_2O/CuO$ Multi-Nanolayers as Sensors for H_2 and Volatile Organic Compounds: An Experimental and Theoretical Investigation, *ACS Appl. Mater. Interfaces*, 2021, **13**, 32363–32380, DOI: 10.1021/acsami.1c04379.

33 O. Lupan, N. Ababii, D. Santos-Carballal, M.-I. Terasa, N. Magariu, D. Zappa, E. Comini, T. Pauporté, L. Siebert, F. Faupel, A. Vahl, S. Hansen, N. H. de Leeuw and R. Adelung, Tailoring the selectivity of ultralow-power heterojunction gas sensors by noble metal nanoparticle functionalization, *Nano Energy*, 2021, **88**, 106241, DOI: 10.1016/j.nanoen.2021.106241.

34 M. Zhao, R. Nitta, S. Izawa, J. Ichi Yamaura and Y. Majima, Nano-Patterned CuO Nanowire Nanogap Hydrogen Gas Sensor with Voids, *Adv. Funct. Mater.*, 2024, **35**, 2415971, DOI: 10.1002/adfm.202415971.

35 R. Molavi and M. H. Sheikhi, Facile wet chemical synthesis of Al doped CuO nanoleaves for carbon monoxide gas sensor applications, *Mater. Sci. Semicond. Process.*, 2020, **106**, 104767.

36 M. Poloju, N. Jayababu and M. V. Ramana Reddy, Improved gas sensing performance of Al doped ZnO/CuO nanocomposite based ammonia gas sensor, *Mater. Sci. Eng., B*, 2018, **227**, 61–67.

37 City rating, https://www.cityrating.com/relativehumidity.asp, (accessed 24 March 2025).

38 A. Wypych, B. Bochenek and M. Różycki, Atmospheric Moisture Content over Europe and the Northern Atlantic, *Atmosphere*, 2018, **9**, 18, DOI: 10.3390/atmos9010018.

39 impact of humidity electronics manufacturing,pdf, https://airinnovations.com/blog/humidity-impact-electronics-manufacturing/, (accessed 15 April 2025).

40 S. Kleszcz and M. Assadi, Hydrogen safety considerations: Mitigating risks and securing operations in enclosed spaces, *IOP Conf. Ser.: Mater. Sci. Eng.*, 2023, **1294**, 12057.

41 O. Lupan, N. Ababii, A. K. Mishra, M. T. Bodduluri, N. Magariu, A. Vahl, H. Krüger, B. Wagner, F. Faupel, R. Adelung, N. H. de Leeuw and S. Hansen, Heterostructure-based devices with enhanced humidity stability for H_2 gas sensing applications in breath tests and portable batteries, *Sens. Actuators, A*, 2021, **329**, 112804.

42 R. G. Pavelko, A. A. Vasiliev, E. Llobet, X. Vilanova, V. G. Sevastyanov and N. T. Kuznetsov, Selectivity problem

of metal oxide based sensors in the presence of water vapors, *Procedia Eng.*, 2010, **5**, 111–114.
43 J.-R. Li, R. J. Kuppler and H.-C. Zhou, Selective gas adsorption and separation in metal–organic frameworks, *Chem. Soc. Rev.*, 2009, **38**, 1477–1504.
44 J. Ding, L. Zhong, X. Wang, L. Chai, Y. Wang, M. Jiang, T.-T. Li, Y. Hu, J. Qian and S. Huang, General approach to MOF-derived core-shell bimetallic oxide nanowires for fast response to glucose oxidation, *Sens. Actuators, B*, 2020, **306**, 127551.
45 J. Xue, C. Han, Y. Yang, S. Xu, Q. Li, H. Nie, J. Qian and Z. Yang, Partially Oxidized Carbon Nanomaterials with Ni/NiO Heterostructures as Durable Glucose Sensors, *Inorg. Chem.*, 2023, **62**, 3288–3296.
46 K. Zhang, R. P. Lively, C. Zhang, R. R. Chance, W. J. Koros, D. S. Sholl and S. Nair, Exploring the Framework Hydrophobicity and Flexibility of ZIF-8: From Biofuel Recovery to Hydrocarbon Separations, *J. Phys. Chem. Lett.*, 2013, **4**, 3618–3622.
47 T. Zhou, Y. Sang, X. Wang, C. Wu, D. Zeng and C. Xie, Pore size dependent gas-sensing selectivity based on ZnO@ZIF nanorod arrays, *Sens. Actuators, B*, 2018, **258**, 1099–1106.
48 R. Lv, Q. Zhang, W. Wang, Y. Lin and S. Zhang, ZnO@ZIF-8 Core-Shell Structure Gas Sensors with Excellent Selectivity to H_2, *Sensors*, 2021, **21**(12), 4069, DOI: **10.3390/s21124069**.
49 S. E. Henkelis, S. J. Percival, L. J. Small, D. X. Rademacher and T. M. Nenoff, Continuous MOF Membrane-Based Sensors via Functionalization of Interdigitated Electrodes, *Membranes*, 2021, **11**(3), 176, DOI: **10.3390/membranes11030176**.
50 H. Yuan, J. Tao, N. Li, A. Karmakar, C. Tang, H. Cai, S. J. Pennycook, N. Singh and D. Zhao, On-Chip Tailorability of Capacitive Gas Sensors Integrated with Metal–Organic Framework Films, *Angew. Chem., Int. Ed.*, 2019, **58**, 14089–14094.
51 M. A. Andrés, M. T. Vijjapu, S. G. Surya, O. Shekhah, K. N. Salama, C. Serre, M. Eddaoudi, O. Roubeau and I. Gascón, Methanol and Humidity Capacitive Sensors Based on Thin Films of MOF Nanoparticles, *ACS Appl. Mater. Interfaces*, 2020, **12**, 4155–4162.
52 M. S. More, G. A. Bodkhe, F. Singh, B. N. Dole, T. Hianik and M. D. Shirsat, Chemiresistive Sensor Based on Metal Organic Framework-Reduced Graphene Oxide (Cu-BTC@rGO) Nanocomposite for the Detection of Ammonia, *Eng. Proc.*, 2023, **48**(1), 32, DOI: **10.3390/CSAC2023-14882**.
53 O. Lupan, V. Cretu, V. Postica, N. Ababii, O. Polonskyi, V. Kaidas, F. Schütt, Y. K. Mishra, E. Monaico, I. Tiginyanu, V. Sontea, T. Strunskus, F. Faupel and R. Adelung, Enhanced ethanol vapour sensing performances of copper oxide nanocrystals with mixed phases, *Sens. Actuators, B*, 2016, **224**, 434–448, DOI: **10.1016/j.snb.2015.10.042**.
54 V. Cretu, V. Postica, A. K. Mishra, M. Hoppe, I. Tiginyanu, Y. K. Mishra, L. Chow, N. H. de Leeuw, R. Adelung and O. Lupan, Synthesis, characterization and DFT studies of zinc-doped copper oxide nanocrystals for gas sensing applications, *J. Mater. Chem. A*, 2016, **4**, 6527–6539, DOI: **10.1039/C6TA01355D**.
55 D. Litra, M. Chiriac, N. Ababii and O. Lupan, Acetone Sensors Based on Al-Coated and Ni-Doped Copper Oxide Nanocrystalline Thin Films, *Sensors*, 2024, **24**(20), 6550, DOI: **10.3390/s24206550**.
56 V. Postica, I. Hölken, V. Schneider, V. Kaidas, O. Polonskyi, V. Cretu, I. Tiginyanu, F. Faupel, R. Adelung and O. Lupan, Multifunctional device based on ZnO:Fe nanostructured films with enhanced UV and ultra-fast ethanol vapour sensing, *Mater. Sci. Semicond. Process.*, 2016, **49**, 20–33, DOI: **10.1016/j.mssp.2016.03.024**.
57 D. Santos-Carballal, O. Lupan, N. Magariu, N. Ababii, H. Krüger, M. T. Bodduluri, N. H. de Leeuw, S. Hansen and R. Adelung, Al_2O_3/ZnO composite-based sensors for battery safety applications: An experimental and theoretical investigation, *Nano Energy*, 2023, **109**, 108301, DOI: **10.1016/j.nanoen.2023.108301**.
58 A. I. A. Soliman, A. M. A. Abdel-Wahab and H. N. Abdelhamid, Hierarchical porous zeolitic imidazolate frameworks (ZIF-8) and ZnO@N-doped carbon for selective adsorption and photocatalytic degradation of organic pollutants, *RSC Adv.*, 2022, **12**, 7075–7084.
59 P. Kutukov, M. Rumyantseva, V. Krivetskiy, D. Filatova, M. Batuk, J. Hadermann, N. Khmelevsky, A. Aksenenko and A. Gaskov, Influence of Mono- and Bimetallic PtO_x, PdO_x, $PtPdO_x$ Clusters on CO Sensing by SnO_2 Based Gas Sensors, *Nanomaterials*, 2018, **8**(11), 917, DOI: **10.3390/nano8110917**.
60 M. Attwa, A. Said, M. ElGamal, Y. El-Shaer and S. Elbasuney, Bespoke Energetic Zeolite Imidazolate Frameworks-8 (ZIF-8)/Ammonium Perchlorate Nanocomposite: A Novel Reactive Catalyzed High Energy Dense Material with Superior Decomposition Kinetics, *J. Inorg. Organomet. Polym. Mater.*, 2024, **34**, 387–400.
61 S. Sharma and P. Chand, Electrochemical behavior of solvothermally grown ZIF-8 as electrode material for supercapacitor applications, *Mater. Today: Proc.*, 2023, **76**, 125–131.
62 J. Dubrovkin, *Data compression in spectroscopy*, Cambridge Scholars Publishing, 2022.
63 C. Byrne, M. Mazaj and N. Z. Logar, Assessing the heat storage potential of zeolitic imidazolate frameworks (ZIFs) using water and ethanol as working fluids, *Mater. Chem. Phys.*, 2025, **332**, 130143.
64 L. Mishra, V. K. Dwivedi, H. K. Dara, V. K. Chakradhary, S. Ithineni, A. G. Prabhudessai and S. Nehar, Core/Shell-Like Magnetic Structure and Optical Properties in CuO Nanoparticles Synthesized by Green Route, *ACS Sustainable Resour. Manage.*, 2024, **1**, 2472–2481.
65 D. A. Carter and J. E. Pemberton, Raman spectroscopy and vibrational assignments of 1- and 2-methylimidazole, *J. Raman Spectrosc.*, 1997, **28**, 939–946.
66 B. Olaniyan and B. Saha, Comparison of Catalytic Activity of ZIF-8 and Zr/ZIF-8 for Greener Synthesis of Chloromethyl Ethylene Carbonate by CO_2 Utilization, *Energies*, 2020, **13**(3), 521, DOI: **10.3390/en13030521**.
67 J. Liu, Z. Gao, Y. Huang and Y. Song, Structural changes and CO_2 adsorption performance in $Zn_2(BDC)_2DABCO$ metal-organic framework under high-pressure and high-temperature conditions, *Can. J. Chem.*, 2025, **103**, 566–574.

68 J. Li, H. Chang, Y. Li, Q. Li, K. Shen, H. Yi and J. Zhang, Synthesis and adsorption performance of La@ZIF-8 composite metal–organic frameworks, *RSC Adv.*, 2020, **10**, 3380–3390.

69 J. Narimbi, S. Balakrishnan, T. S. Perova, G. Dee, G. F. Swiegers and Y. K. Gun'ko, XRD and Spectroscopic Investigations of ZIF—Microchannel Glass Plates Composites, *Materials*, 2023, **16**(6), 2410, DOI: 10.3390/ma16062410.

70 A. Deacon, L. Briquet, M. Malankowska, F. Massingberd-Mundy, S. Rudić, T. L. Hyde, H. Cavaye, J. Coronas, S. Poulston and T. Johnson, Understanding the ZIF-L to ZIF-8 transformation from fundamentals to fully costed kilogram-scale production, *Commun. Chem.*, 2022, **5**, 18, DOI: 10.1038/s42004-021-00613-z.

71 G. Mani, A. V. Kumar and S. Mathew, ZIF-8 derived ZnO: a facile catalyst for ammonium perchlorate thermal decomposition, *RSC Sustainability*, 2023, **1**, 2081–2091, DOI: 10.1039/d3su00256j.

72 B. Xu, Y. Mei, Z. Xiao, Z. Kang, R. Wang and D. Sun, Monitoring thermally induced structural deformation and framework decomposition of ZIF-8 through in situ temperature dependent measurements, *Phys. Chem. Chem. Phys.*, 2017, **19**, 27178–27183.

73 X. Liu, J. Zhang, Y. Dong, H. Li, Y. Xia and H. Wang, A facile approach for the synthesis of Z-scheme photocatalyst ZIF-8/g-C_3N_4 with highly enhanced photocatalytic activity under simulated sunlight, *New J. Chem.*, 2018, **42**, 12180–12187.

74 A. Awadallah-F, F. Hillman, S. A. Al-Muhtaseb and H.-K. Jeong, On the nanogate-opening pressures of copper-doped zeolitic imidazolate framework ZIF-8 for the adsorption of propane, propylene, isobutane, and *n*-butane, *J. Mater. Sci.*, 2019, **54**, 5513–5527.

75 F. Tian, A. M. Cerro, A. M. Mosier, H. K. Wayment-Steele, R. S. Shine, A. Park, E. R. Webster, L. E. Johnson, M. S. Johal and L. Benz, Surface and Stability Characterization of a Nanoporous ZIF-8 Thin Film, *J. Phys. Chem. C*, 2014, **118**, 14449–14456.

76 J. Qiu, X. Xu, B. Liu, Y. Guo, H. Wang, L. Yu, Y. Jiang, C. Huang, B. Fan, Z. Zeng and L. Li, Size-Controllable Synthesis of ZIF-8 and Derived Nitrogen-Rich Porous Carbon for CO_2 and VOCs Adsorption, *ChemistrySelect*, 2022, **7**, e202203273.

77 Y. Wu, R. Fang, L. Shen and H. Bai, Dual mechanisms in hydrogen reduction of copper oxide: surface reaction and subsurface oxygen atom transfer, *RSC Adv.*, 2024, **14**, 9985–9995.

78 R. Nagpal, C. Lupan, P. Schadte, A. Birnaz, M. Brinza, L. Siebert and O. Lupan, Study on Al_2O_3/ZnO Heterostructure Based UV Detection for Biomedical Applications, Springer Nature Switzerland, *Advances in Digital Health and Medical Bioengineering*, 2024, vol. 111, pp. 178–188, DOI: 10.1007/978-3-031-62523-7_20.

79 W. Mtangi, F. D. Auret, C. Nyamhere, P. J. Janse van Rensburg, A. Chawanda, M. Diale, J. M. Nel and W. E. Meyer, The dependence of barrier height on temperature for Pd Schottky contacts on ZnO, *Phys. B*, 2009, **404**, 4402–4405.

80 X. Meng, M. Bi, Q. Xiao and W. Gao, Ultra-fast response and highly selectivity hydrogen gas sensor based on Pd/SnO_2 nanoparticles, *Int. J. Hydrogen Energy*, 2022, **47**, 3157–3169.

81 P. Shankar and J. B. B. Rayappan, Room temperature ethanol sensing properties of ZnO nanorods prepared using an electrospinning technique, *J. Mater. Chem. C*, 2017, **5**, 10869–10880.

82 C. Gao, J. Wu, Q. Shi, H. Ying and J. Dong, Adsorption breakthrough behavior of 1-butanol from an ABE model solution with high-silica zeolite: Comparison with zeolitic imidazolate frameworks (ZIF-8), *Microporous Mesoporous Mater.*, 2017, **243**, 119–129.

83 I.-K. Cheng, C.-Y. Lin and F.-M. Pan, Gas sensing behavior of ZnO toward H_2 at temperatures below 300 °C and its dependence on humidity and Pt-decoration, *Appl. Surf. Sci.*, 2021, **541**, 148551.

84 T. T. Suzuki, T. Ohgaki, Y. Adachi, I. Sakaguchi, M. Nakamura, H. Ohashi, A. Aimi and K. Fujimoto, Ethanol Gas Sensing by a Zn-Terminated ZnO(0001) Bulk Single-Crystalline Substrate, *ACS Omega*, 2020, **5**, 21104–21112.

85 L. Sui, W. Zhang, P. Wang, B. Zhao, H. Wu, D. Zhao, G. Dong, H. Yu, Y. Xu and L. Huo, A fast response ppb-level aniline gas sensor based on hierarchical hollow spheres of α-Fe_2O_3/α-MoO_3 heterostructure, *Sens. Actuators, B*, 2021, **346**, 130519.

86 G. Ren, Z. Li, W. Yang, M. Faheem, J. Xing, X. Zou, Q. Pan, G. Zhu and Y. Du, ZnO@ZIF-8 core-shell microspheres for improved ethanol gas sensing, *Sens. Actuators, B*, 2019, **284**, 421–427.

87 D. O. Scanlon, B. J. Morgan, G. W. Watson and A. Walsh, Acceptor Levels in p-Type Cu_2O Rationalizing Theory and Experiment, *Phys. Rev. Lett.*, 2009, **103**, 96405.

88 G. K. Paul, Y. Nawa, H. Sato, T. Sakurai and K. Akimoto, Defects in Cu_2O studied by deep level transient spectroscopy, *Appl. Phys. Lett.*, 2006, **88**, 141901.

89 F. de Souza Lucas, H. Peng, S. Johnston, P. C. Dippo, S. Lany, L. H. Mascaro and A. Zakutayev, Characterization of defects in copper antimony disulfide, *J. Mater. Chem. A*, 2017, **5**, 21986–21993.

90 S. S. Nair, N. Illyaskutty, B. Tam, A. O. Yazaydin, K. Emmerich, A. Steudel, T. Hashem, L. Schöttner, C. Wöll, H. Kohler and H. Gliemann, ZnO@ZIF-8: Gas sensitive core-shell hetero-structures show reduced cross-sensitivity to humidity, *Sens. Actuators, B*, 2020, **304**, 127184.

91 IUPAC analytical compendium.

92 Á. Peña, D. Matatagui, F. Ricciardella, L. Sacco, S. Vollebregt, D. Otero, J. López-Sánchez, P. Marín and M. C. Horrillo, Optimization of multilayer graphene-based gas sensors by ultraviolet photoactivation, *Appl. Surf. Sci.*, 2023, **610**, 155393.

93 X. Zhang, J. Sun, K. Tang, H. Wang, T. Chen, K. Jiang, T. Zhou, H. Quan and R. Guo, Ultralow detection limit and ultrafast response/recovery of the H_2 gas sensor based on Pd-doped rGO/ZnO–SnO_2 from hydrothermal synthesis, *Microsyst. Nanoeng.*, 2022, **8**, 67, DOI: **10.1038/s41378-022-00398-8**.

94 M. Zhou, F. Guo, F. Duanmu and Z. Shen, Enhanced sensing performance toward alcohols using copper oxide based on exposed crystal facet driven catalytic oxidation, *J. Mater. Sci.: Mater. Electron.*, 2021, **32**, 26676–26687.

95 N. H. Al-Hardan, M. J. Abdullah and A. A. Aziz, Sensing mechanism of hydrogen gas sensor based on RF-sputtered ZnO thin films, *Int. J. Hydrogen Energy*, 2010, **35**, 4428–4434.

96 R. Lv, Q. Zhang, W. Wang, Y. Lin and S. Zhang, ZnO@ZIF-8 Core-Shell Structure Gas Sensors with Excellent Selectivity to H_2, *Sensors*, 2021, **21**(12), 406, DOI: **10.3390/s21124069**.

97 Y. Wu, R. Fang, L. Shen and H. Bai, Dual mechanisms in hydrogen reduction of copper oxide: surface reaction and subsurface oxygen atom transfer, *RSC Adv.*, 2024, **14**, 9985–9995.

98 M. H. Yamukyan, Kh. V. Manukyan and S. L. Kharatyan, Copper oxide reduction by hydrogen under the self-propagation reaction mode, *J. Alloys Compd.*, 2009, **473**, 546–549.

99 A. Schlaich, J. L. Barrat and B. Coasne, Theory and Modeling of Transport for Simple Fluids in Nanoporous Materials: From Microscopic to Coarse-Grained Descriptions, *Chem. Rev.*, 2025, **125**(5), 2561–2624, DOI: **10.1021/acs.chemrev.4c00406**.

100 V. A. Tuan, S. Li, J. L. Falconer and R. D. Noble, In Situ Crystallization of Beta Zeolite Membranes and Their Permeation and Separation Properties, *Chem. Mater.*, 2002, **14**, 489–492.

101 C. Gao, Q. Shi and J. Dong, Adsorptive separation performance of 1-butanol onto typical hydrophobic zeolitic imidazolate frameworks (ZIFs), *CrystEngComm*, 2016, **18**, 3842–3849.

102 M. Gussoni, M. Rui and G. Zerbi, Electronic and relaxation contribution to linear molecular polarizability. An analysis of the experimental values, *J. Mol. Struct.*, 1998, **447**, 163–215, DOI: **10.1016/S0022-2860(97)00292-5**.

103 J. Cousin Saint Remi, T. Rémy, V. Van Hunskerken, S. van de Perre, T. Duerinck, M. Maes, D. De Vos, E. Gobechiya, C. E. A. Kirschhock, G. V. Baron and J. F. M. Denayer, Biobutanol Separation with the Metal–Organic Framework ZIF-8, *ChemSusChem*, 2011, **4**, 1074–1077, DOI: **10.1002/cssc.201100261**.

104 O. Lupan, R. Nagpal, D. Litra, M. Brinza, M. Sugihara, R. Ameloot, S. Railean, T. Ameri, R. Adelung, S. Schröder and F. Faupel, Hybrid Nanomaterials for Biomedical Sensors, *7th International Conference on Nanotechnologies and Biomedical Engineering. ICNBME 2025. IFMBE Proceedings*, 2025, **134**, 162–176, DOI: **10.1007/978-3-032-06494-3_18**.